HCN channel-mediated neuromodulation can control action potential velocity and fidelity in central axons

Niklas Byczkowicz[1], Abdelmoneim Eshra[1], Jacqueline Montanaro[2], Andrea Trevisiol[3], Johannes Hirrlinger[1,3], Maarten H. P. Kole[4,5], Ryuichi Shigemoto[2], and Stefan Hallermann[1,#]

[1] Carl-Ludwig-Institute for Physiology, Medical Faculty, University of Leipzig, Liebigstr. 27, 04103 Leipzig, Germany
[2] Institute of Science and Technology Austria (IST Austria), Am Campus 1, 3400 Klosterneuburg, Austria
[3] Department of Neurogenetics, Max-Planck-Institute for Experimental Medicine, Hermann-Rein-Strasse 3, 37075 Göttingen, Germany
[4] Department of Axonal Signaling, Netherlands Institute for Neuroscience, Royal Netherlands Academy of Arts and Sciences, Meibergdreef 47, 1105 BA, Amsterdam, Netherlands.
[5] Cell Biology, Faculty of Science, University of Utrecht, Padualaan 8, 3584 CH, The Netherlands.
[#] Correspondence: hallermann@medizin.uni-leipzig.de

Abstract

Hyperpolarization-activated cyclic-nucleotide-gated (HCN) channels control electrical rhythmicity and excitability in the heart and brain, but the function of HCN channels at subcellular level in axons remains poorly understood. Here, we show that the action potential conduction velocity in both myelinated and unmyelinated central axons can bidirectionally be modulated by HCN channel blockers, cyclic adenosine monophosphate (cAMP), and neuromodulators. Recordings from mice cerebellar mossy fiber boutons show that HCN channels ensure reliable high-frequency firing and are strongly modulated by cAMP (EC_{50} 40 µM; estimated endogenous cAMP concentration 13 µM). In accord, immunogold-electron microscopy revealed HCN2 as the dominating subunit in cerebellar mossy fibers. Computational modeling indicated that HCN2 channels control conduction velocity primarily via altering the resting membrane potential and was associated with significant metabolic costs. These results suggest that the cAMP-HCN pathway provides neuromodulators an opportunity to finely tune energy consumption and temporal delays across axons in the brain.

Introduction

HCN channels are expressed in the heart and nervous system and comprise four members (HCN1–HCN4) differing in their kinetics, voltage-dependence and degree of sensitivity to cyclic nucleotides such as cAMP (Biel et al., 2009; Robinson and

Siegelbaum, 2003). Membrane hyperpolarization activates HCN channels and causes a depolarizing mixed sodium/potassium (Na^+/K^+) current. In the heart, the current through HCN channels (I_f) mediates the acceleratory effect of adrenaline on heart rate by direct binding of cAMP (DiFrancesco, 2006). In neurons, the current through HCN channels (I_h) controls a wide array of functions, such as rhythmic activity (Pape and McCormick, 1989) and excitability (Tang and Trussell, 2015). In addition to the somatic impact, HCN channels are expressed throughout various subcellular compartments of neurons (Nusser, 2012). For example, patch-clamp recordings from dendrites in pyramidal neurons have revealed particularly high densities of HCN channels which acts to control the local resting potential and leak conductance, thereby playing important roles in regulating synaptic integration (George et al., 2009; Harnett et al., 2015; Kole et al., 2006; Magee, 1999; Williams and Stuart, 2000).

In contrast, the expression and role of I_h in the axon is less studied and may vary with species. I_h seems to critically control the strength of synaptic transmission in crayfish and *Drosophila* neuromuscular junction (Beaumont and Zucker, 2000; Cheung et al., 2006). However, presynaptic recordings from the vertebrate calyx of Held in the auditory brainstem found I_h to marginally affect neurotransmitter release (Cuttle et al., 2001), but to exert a strong influence on the resting membrane potential (Cuttle et al., 2001; Kim and von Gersdorff, 2012) and vesicular neurotransmitter uptake (Huang and Trussell, 2014). At synaptic terminals of pyramidal neurons in the cortex of mice, HCN channels inhibit glutamate release by suppressing the activity of T-type Ca^{2+} channels (Huang et al., 2011).

Besides a potential impact on neurotransmitter release, axonal I_h could play a role in the propagation of action potentials. Indeed, in axons of the stomatogastric nervous system of lobsters (Marder and Bucher, 2001) it was shown that the action potential conduction was affected by dopamine via axonal HCN channels (Ballo et al., 2010; Ballo et al., 2012). In vertebrates, studies on action potential propagation by Waxman and coworkers indicated that I_h counteracts the hyperpolarization of the membrane potential during periods of high-frequency firing (Baker et al., 1987; Birch et al., 1991; Waxman et al., 1995) and that it participates in ionic homeostasis at the node of Ranvier

(Waxman and Ritchie, 1993). More recent investigations found I_h to be crucial for the emergence of persistent action potential firing in axons of parvalbumin-positive interneurons (Elgueta et al., 2015), but I_h seems to have an opposing effect on the excitability at the axon initial segment, where its activation reduces the probability of action potential initiation (Ko et al., 2016). Finally, there is evidence from extracellular recordings that blocking I_h decreases the action potential conduction velocity in unmyelinated central (Baginskas et al., 2009; Soleng et al., 2003) and peripheral axons of vertebrates (Grafe et al., 1997). However, neuromodulation of conduction velocity and the underlying cellular membrane mechanisms are not known in vertebrate axons.

Here, we demonstrate a decrease or increase in conduction velocity in central axons through the application of HCN blockers or neuromodulators. To gain mechanistic insights into the modulation of conduction velocity by HCN channels, we performed recordings from *en passant* cerebellar mossy fiber boutons (cMFB; Ritzau-Jost et al., 2014; Delvendahl et al., 2015). We found that HCN channels in cMFBs mainly consist of the HCN2 subunit, are ~7% activated at resting membrane potential, ensure high-frequency firing, and control the passive membrane properties. Whole-cell and perforated patch clamp recordings from cMFBs demonstrated a strong dependence of HCN channels on intracellular cAMP concentration with an EC_{50} of 40 µM and a high endogenous cAMP concentration of 13 µM. Computational modelling indicated that the resting membrane potential controls conduction velocity and that the activity of HCN channel is metabolically expensive. These data reveal a mechanism shared among different types of axons to bidirectionally modulate conduction velocity in the central nervous system.

Results

Bidirectional modulation of conduction velocity

To investigate whether HCNs affect conduction velocity, we recorded compound action potentials in three different types of axons (Fig. 1): Application of the specific HCN channel blocker ZD7288 (30 µM) decreased the conduction velocity by 8.0 ± 2.8% in myelinated cerebellar mossy fibers (n = 14), by 9.2 ± 0.9% in non-myelinated cerebellar parallel fibers (n = 15), and by 4.0 ± 0.8% in optical nerves (n = 4; see Fig. 1 and legend

for statistical testing). Since some studies implied that ZD7288 might have some unspecific side effects, such as blocking voltage-dependent Na^+ channels (Chevaleyre and Castillo, 2002; Wu et al., 2012), we recorded Na^+ currents from 53 cMFBs and found no change in amplitude or kinetics of voltage-dependent Na^+ currents after ZD7288 application (Supplemental Fig. 1), suggesting that under our conditions and at a concentration of 30 µM, ZD7288 did not affect the Na^+ currents. Because of the modulation of HCN channels by intracellular cAMP, we measured conduction velocity during application of 8-bromoadenosine 3′,5′-cyclic monophosphate (8-Br-cAMP; 500 µM), a membrane-permeable cAMP-analogue. The conduction velocity increased by 5.9 ± 2.8% in cerebellar mossy fibers (n = 17), by 3.7 ± 1.4% in parallel fibers (n = 10), and by 4.6 ± 0.6% in optic nerves (n = 5; see Fig. 1 and legend for statistical testing). These results indicate that HCN channels control the conduction velocity both in myelinated and non-myelinated central axons.

Neuromodulators differentially regulate conduction velocity

To investigate a modulation of conduction velocity by physiological neuromodulators, we focused on the cerebellar parallel fibers, where the velocity could be most accurately measured, and then applied several modulators known to act via cAMP-dependent pathways (Fig. 2). Wash-in of 200 µM norepinephrine (NE) resulted in a relatively fast increase in conduction velocity (1.9 ± 0.8%; n = 6; see Fig. 2B and legend for statistical testing), consistent with the existence of β-adrenergic receptors in the cerebellar cortex (Nicholas et al., 1993), which increase the cAMP concentration via G_s-proteins. On the other hand, the application of either 200 µM serotonin (–3.5 ± 0.5%; n = 11), 200 µM dopamine (–5.0 ± 0.7%; n = 13) or 200 µM adenosine (–7.2 ± 0.6%; n = 5) resulted in a continuous decrease of the conduction velocity (Fig. 2B and C; see legend for statistical testing), consistent with the existence of G_i-coupled receptors for serotonin, dopamine, and adenosine in the molecular layer of the cerebellum (Geurts et al., 2002; Schweighofer et al., 2004), which decrease the cAMP concentration. Although we used rather high concentrations of the agonists and off-target effects cannot be excluded (e.g., NE activating dopamine receptors; Sánchez-Soto et al., 2016), these data nevertheless indicate that physiological neuromodulators can both increase or decrease action potential conduction velocity, depending on the type of neuromodulator and receptor.

Neuromodulation of conduction velocity is mediated by HCN channels

In addition to HCN channels, some voltage gated Na^+, K^+, and Ca^{2+} channels can be modulated via the intracellular cAMP-pathway (Burke et al., 2018; Yang et al., 2013; Yin et al., 2017). To address the contribution of other channels on the neuromodulation of the conduction velocity, we performed a set of experiments, in which HCN channels were first blocked by 30 µM ZD7288 and subsequently three modulatory substances that significantly increased or decreased conduction velocity in prior experiments were applied. With ZD7288 continuously being present in the recording solution, conduction velocity of parallel fibers slightly decreased over the course of 20 minutes (Fig. 3A). Adding 8Br-cAMP (500 µM), Adenosine (200 µM) or NE (100 µM) at t = 5 min (i.e. 25 minutes after application of ZD7288) did not change the conduction velocity significantly compared with control (only ZD7288). The average conduction velocity between t = 15 and 20 min was decreased by –3.3 ± 2.4% for cAMP (n = 9), –4.6 ± 1.6% for Adenosine (n = 9) and –3.7 ± 1.2% for NE (n = 7), compared to the average velocity between t = 0 and 5 min baseline recording. This was not significantly different from the decrease in the sole presence of ZD7288 (–3.3 ± 1.4%; n = 7, see Fig. 3B and legend for statistical testing), indicating that the previously shown effects of cAMP and neuromodulators on conduction velocity are mainly mediated by HCN channels.

Cerebellar mossy fiber terminals have a prominent voltage sag

To investigate the membrane and signaling mechanisms underlying the bidirectional control of conduction velocity, we focused on cerebellar mossy fibers, which allow the whole-cell recording configuration and a direct access to the cytoplasmic compartment (Fig. 4A). Recordings from *en passant* cMFBs are well suited to investigate the ionic basis of conduction velocity in the adjacent axonal compartments, because of a long membrane length constant and slow HCN channel gating. Injection of depolarizing currents during current-clamp recordings evoked a single action potential and injection of hyperpolarizing currents generated a substantial ‘sag’ at cMFBs (Fig. 4B; Rancz et al., 2007; Ritzau-Jost et al., 2014), i.e. a delayed depolarization towards the resting potential, which is a hallmark of the presence of I_h (Biel et al., 2009; Robinson and Siegelbaum, 2003). At a potential of on average –150 mV, the sag ratio, calculated from

the peak and steady state amplitude as indicated in Fig. 4C (George et al., 2009), was 0.497 ± 0.030 (n = 12).

HCN channels support high frequency action potential firing

Using direct presynaptic recordings from cMFBs, we first aimed to investigate the impact of HCN channels on action potential firing. To this end, we analyzed action potentials elicited by current injections into the cMFBs (data not shown) as well as traveling action potentials elicited by axonal stimulation with a second pipette (Fig. 5A). In both cases, the amplitude and half-duration of action potentials elicited at 1 Hz were not significantly affected by application of 30 µM ZD7288 (data not shown and Fig. 5B and C, respectively), indicating that HCN channels do not alter the active membrane properties profoundly.

However, cerebellar mossy fibers can conduct trains of action potentials at frequencies exceeding 1 kHz (Ritzau-Jost et al., 2014), making them an ideal target to study the impact of axonal HCNs on the propagation of high-frequency action potentials as well. Blocking HCN channels significantly impaired the ability of mossy fibers to fire at high frequencies (20 action potentials at 200 – 1666 Hz). In the examples illustrated in Fig. 5D, the failure-free trains of action potentials could be elicited at up to 1.1 kHz under control conditions and up to 500 Hz, when ZD7288 was present in the extracellular solution. The average failure-free frequency reduced from 854 ± 60 in control to 426 ± 63 Hz in the presence of ZD7288 (n = 20 and 10, respectively; $P_{T\text{-}Test}$ = 0.0002; Fig. 5E). Action potential broadening and amplitude reduction was more pronounced in the presence of ZD7288. For example, during trains of action potentials at 200 Hz, the half-duration of the 20th action potential was 109.6 ± 1.5 and 141.7 ± 7.0% of the half-duration of the 1st action potential for control and ZD7288, respectively (n = 20 and 10; $P_{T\text{-}Test}$ = 0.02; Fig. 5E). The amplitude of the 20th action potential was 96.5 ± 0.8 and 82.9 ± 1.6% of the 1st action potential for control and ZD7288, respectively (n = 20 and 10; $P_{T\text{-}Test}$ = 0.02; Fig. 5E). Furthermore, the delay during trains of action potentials at 200 Hz increased by ~20% in the presence of ZD7288 but decreased by ~5% in control recordings (Fig. 5F), indicating an acceleration and a slowing of conduction velocity during high-frequency firing for control and ZD7288, respectively. The difference in

delay of the 20th action potential was maximal at intermediate frequencies (200 and 333 Hz; Fig. 5G). These experiments show, that HCNs, despite their slow kinetics, ensure reliable high-frequency firing.

The passive membrane properties of cMFBs are HCN- and cAMP-dependent

To better understand how I_h impacts action potential firing, we next investigated the passive membrane properties of cMFBs by recording the voltage response elicited by small hyperpolarizing current injections (–10 pA for 300 ms) in the absence and presence of 30 µM ZD7288 (Fig. 6A and B). ZD7288 caused a hyperpolarization of the resting membrane potential by, on average, 5.4 mV (–80.0 ± 0.6 mV and –85.4 ± 1.4 mV for control and ZD7288, n = 94 and 35, respectively), a doubling of the apparent input resistance calculated from the steady state voltage at the end of the current step (794 ± 48 MΩ and 1681 ± 185 MΩ), as well as a doubling of the apparent membrane time constant, as determined by a mono-exponential fit to the initial decay of the membrane potential (14.4 ± 0.8 ms and 35.0 ± 2.5 ms, respectively; see legend of Fig. 6B for statistical testing). To analyze the cAMP-dependence of the conduction velocity (cf. Fig. 1), we determined the cAMP-dependence of the passive membrane properties of cMFBs. Adding cAMP in various concentrations to the intracellular solution depolarized the membrane potential and decreased both the input resistance and the apparent membrane time constant in a concentration-dependent manner, which shows an opposite effect compared to the application of ZD7288 (Fig. 6B). These data suggest that HCN channels in cerebellar mossy fibers determine the passive membrane properties as a function of the intracellular cAMP concentration.

HCN2 is uniformly distributed in mossy fiber axons and boutons

Of the four HCN subunits (HCN1–HCN4), the subunits HCN1 and HCN2 are predominantly expressed in the cerebellar cortex (Notomi and Shigemoto, 2004; Santoro et al., 2000). Previous studies in the cortex, hippocampus, and auditory brainstem primarily detected HCN1 in axons (Elgueta et al., 2015; Huang et al., 2011; Ko et al., 2016), but HCN2 was found to be more sensitive to cAMP in comparison to HCN1 (Wang et al., 2001; Zagotta et al., 2003). To understand the pronounced cAMP dependence of conduction velocity (cf. Fig. 1) and passive membrane properties (cf.

Fig. 6) at the molecular level, we investigated the identity and distribution of HCN channels using pre-embedding immunogold labeling for HCN1 and 2 in cMFBs and adjacent axons. At the electron microscopic level, we found only background immunoreactivity for HCN1 (data not shown) but significant labeling for HCN2 (Fig. 7A). HCN2 immunogold particles were diffusely distributed along the plasma membrane of cMFBs, with similar labeling density in the adjacent mossy fiber axon (Fig. 7B), which could be traced back up to 3.5 µm from cMFBs. In addition, we created a 3D reconstruction of a cMFB (Fig. 7C and Supplemental Video), including gold particles for HCN2 and identified synaptic connections. While synapses onto granule cell dendrites were observed within invaginated parts of the bouton, HCN2 was uniformly distributed without apparent spatial relations within those synapses. The density of immunogold particles for HCN2 in this reconstructed bouton was 17.1 particles/µm^2 (in total 1260 particles per 73.65 µm^2). The mean density of immunogold particles for HCN2 was 22.7 ± 2.4 per µm^2 (n = 6 cMFBs from 2 mice). These data indicate that HCN2 is the dominant subunit mediating I_h in cMFBs, consistent with its pronounced cAMP-dependence.

HCN channels in cMFB are strongly modulated by cAMP

To better understand the function of axonal HCN2 channels and their modulation by intracellular cAMP, we performed voltage-clamp recordings from cMFBs combined with different cAMP concentrations within the intracellular patch solution. Hyperpolarizing voltage steps evoked a slowly activating, non-inactivating inward current, which was inhibited by ZD7288 (Fig. 8A). Using tail currents of ZD7288-sensitive currents evoked by voltage steps between –80 mV and –150 mV from a holding potential of –70 mV, we calculated the activation curve of I_h with a mean $V_{½}$ of –103.3 ± 0.8 mV (Fig. 8B; n = 36 $V_{½}$-values, each from a different cMFB). Based on the average resting membrane potential of cMFBs, this means about 7% of the overall HCN2-mediated current is active at rest.

To analyze the cAMP concentration-dependence of I_h, we added different concentrations of cAMP (30 µM to 10 mM) to the intracellular patch solution. With 1 mM cAMP $V_{½}$ shifted by 17 mV to on average –86.6 ± 1.2 mV (n = 16 cMFBs; $P_{T\text{-}Test}$ <

10^{-10}; Fig. 8B). The resulting average shifts of $V_{½}$ revealed an EC_{50} of 40.4 µM intracellular cAMP (Fig. 8D). In order to estimate the endogenous presynaptic cAMP concentration, we performed presynaptic perforated-patch recordings on cMFBs. Under perforated patch conditions, $V_{½}$ of I_h was –96.4 ± 1.2 mV (n = 10), significantly more depolarized compared to the corresponding whole-cell recordings after rupturing of the perforated patch (–101.3 ± 1.0 mV; n = 15; $P_{T\text{-}Test}$ = 0.0076; Fig. 8C; see methods for comparison with addition control groups). This voltage shift indicates an endogenous cAMP concentration of 12.6 µM in cMFBs, with a 68%-confidence interval of 1.8 to 60.7 µM cAMP (Fig. 8D). These data reveal a high endogenous resting cAMP concentration.

Hodgkin-Huxley model describing HCN2 channel gating

For our ultimate aim, to obtain a mechanistic and quantitative understanding of axonal HCN2 function in cerebellar mossy-fiber axons, we developed a computational Hodgkin-Huxley (HH) model. The model was constrained to the experimentally recorded I_h kinetics derived from the activation and deactivation time constants of I_h (Fig. 9A) measured at potentials between –70 and –150 mV. The activation curve (cf. Fig. 9B), as well as the averaged time constants for both activation (n = 20) and deactivation (n = 15; Fig. 9B) were well described by a HH-model with one activation gate. In addition, we generated an alternative HH-model to describe the HCN2 current in the presence of 1 mM intracellular cAMP (for a more detailed implementation of the cAMP-dependence of HCN2 gating see Hummert et al., 2018). Furthermore, we estimated the reversal potential of I_h with short voltage ramps as described previously (Cuttle et al., 2001) and found a value of –23.4 ± 1.4 mV (n = 7; Fig. 9C), similar to previous estimates (Aponte et al., 2006; Cuttle et al., 2001). These data provide a quantitative description of axonal I_h at cMFBs.

Mechanism of conduction velocity-control and metabolic costs of HCN channels

What are the mechanisms by which axonal HCN2 channels control conduction velocity? In principle, the depolarization caused by HCN2 channels will bring the resting membrane potential closer to the threshold of voltage-gated Na^+ channel activation, which could accelerate the initiation of the action potential (see discussion).

Alternatively, the increased membrane conductance caused by HCN2 channels will decrease the membrane time constant, which could accelerate the voltage responses, as has been shown, e.g., for dendritic signals in auditory pathways (Golding and Oertel, 2012; Mathews et al., 2010). To distinguish between these two possibilities, we generated a conductance-based NEURON model consisting of cylindrical compartments representing cMFBs connected by myelinated axons (Fig. 10A; Ritzau-Jost et al., 2014). The model contained voltage-dependent axonal Na^+ and K^+ channels, passive Na^+ and K^+ leak channels, and the established HH model of I_h (cf. Fig. 9). After adjustments of the peak conductance densities the model captured the current clamp responses to –10 pA current injections (Fig. 10B), the resting membrane potential (Fig. 10C) as well as the apparent input resistance (Fig. 10D). Removing the HH model of I_h or replacing it with the 1-mM-cAMP-HH-model of I_h, reproduced the corresponding voltage responses, the shift in the resting membrane potential, and the change in the apparent input resistance obtained in the presence of ZD7288 or 1 mM intracellular cAMP (Fig. 10B-D). Interestingly, the models predicted a decrease of the conduction velocity when the control HH model was removed and, conversely, an increase with the 1-mM-cAMP-HH model (Fig. 10E), to a similar extent as experimentally measured with ZD7288 and 8-Br-cAMP (cf. Fig. 1). These findings support our conclusion that HCN2 channel modulation suffices to bi-directionally tune conduction velocity.

Next, we generated two additional models, in which either only the depolarizing effect of HCN2 channels (V_m-*model*) or the decreased input resistance, i.e. the decreased membrane resistance (R_m-*model*) was implemented (by modifying the K^+ or the I_h reversal potential, respectively, see methods). The results showed that the V_m-*model* but not the R_m-*model* caused an increase in conduction velocity, indicating that the depolarizing effect of axonal HCN2 channels determines conduction velocity (Fig. 10E). Interestingly, increasing the resting membrane potential from –90 to –65, decreased the availability of voltage dependent Na^+ (Na_V) channels but increased the conduction velocity (Fig. S2). Only at resting membrane potentials above –65 mV the conduction velocity decreased in our model. Together, these data indicate that the depolarization mediated by HCN2 channels accelerates the conduction velocity by bringing the membrane potential closer to the firing threshold.

The non-inactivating nature of HCN channels and the accompanying shunt at the resting membrane potentials suggest that I_h is metabolically expensive. Therefore, we calculated the Na^+ influx in each model and converted it into the required ATP consumption to restore the Na^+ gradient (Hallermann et al., 2012). Computational modeling showed that it is ~100% more expensive to maintain the resting membrane potential with I_h than without or by depolarization alone (*V_m-model*; Fig. 10F). Furthermore, the metabolic costs to maintain the resting membrane potential with I_h for one second was ~3-fold higher than the costs to generate one action potential (Fig. 10F). Assuming an average frequency of cerebellar mossy fibers of 4 Hz *in vivo* (Chadderton et al.; Rancz et al., 2007), the HCN2 channels increased the required energy of cerebellar mossy fibers by ~30%. With increasing firing frequency, the metabolic costs of action potential firing will become dominating compared with the HCN2-mediated costs for resting membrane potentials (e.g., ~3% at 40 Hz). These data indicate that HCN2 channels are a major contribution for the energetic demands of axons.

Discussion

Here, we demonstrate that the presence of HCN channels in axons accelerates conduction velocity in various types of central axons and that neuromodulators change axonal conduction velocity. By combining advanced electrophysiological, electron-microscopic, and computational techniques, we reveal the mechanism and the metabolic costs of the dynamic control of axonal conduction velocity by HCN channels in the vertebrate central nervous system.

Dynamic control of conduction velocity

We describe both an increase and decrease of the baseline axonal conduction velocity in the range of ~5% mediated by HCN channels (Figs. 1 – 3). Furthermore, HCN channel accelerate action potential propagation by ~25% and increase the maximal failure-free firing frequency by a factor of 2. Although the changes in baseline conduction velocity are relatively small, considering the long distances that axons traverse in the brain, HCN channels can be expected to change the arrival time of the action potential by for example 0.5 ms in the case of cerebellar parallel fibers (assuming 3 mm length and 0.3

m/s velocity; see also Swadlow and Waxman, 2012). Such temporal delays will influence information processing in the central nervous system, because spike-timing dependent plasticity (Caporale and Dan, 2008), coincidence detection (Softky, 1994), and neuronal rhythms of cell ensembles (Buzsáki et al., 2013) precisely tune the arrival times of action potentials. There are several examples for specific tuning of conduction velocity in the sub-millisecond domain: the diameter and the degree of myelination of cerebellar climbing fibers (Sugihara et al., 1993; Lang and Rosenbluth, 2003; but see Baker and Edgley, 2006), the degree of myelination of thalamocortical axons (Salami et al., 2003), and the internode distance of auditory axons (Ford et al., 2015) are tuned to exactly offset different arrival times of action potentials with a temporal precision of ~100 µs.

The cerebellum is involved in the accurate control of muscle contraction with a temporal precision of 1-100 ms (Hore et al., 1991). Submillisecond correlations in spike timing occuring between neighboring Purkinje cells have been noted previously (reviewed in Isope et al., 2002; Person and Raman, 2012). Furthermore, submillisecond precision of the mossy/parallel fiber input are critical for information processing in the cerebellar circuits (Braitenberg et al., 1997; Heck et al., 2001). Together, the here-described changes in action potential conduction velocity in mossy and parallel fibers (Figs. 1-3) may thus play an important role in cerebellar computation. Furthermore, the observed impairment in high-frequency firing without HCN channels (Fig. 5) is expected to negatively impact such functions (Delvendahl and Hallermann, 2016).

Our findings that the cAMP-HCN pathway and neuromodulators can finely tune conduction velocity in the vertebrate central nervous system adds to the emerging idea that axons directly contribute to computation in neuronal circuits. Indeed, the view of the axon as a simple and cable-like compartment in which conduction velocity is static has substantially changed over the recent years in favor for a model that allows flexibility and complex forms of axonal computation (Debanne et al., 2011). Recent findings showed that axon diameters change during the time scales of LTP induction (Chéreau et al., 2017) and changes in myelination in the motor cortex were resolved during learning of complex motor skills (McKenzie et al., 2014; for environmental

effects on myelination see also Forbes and Gallo, 2017). One caveat of our study, is the rather high concentrations of the used neuromodulators and the lack of *in vivo* evidence for neuromodulation of conduction velocity. However, our data demonstrate that under certain conditions an active control of conduction velocity could occur in the vertebrate CNS via the cAMP-HCN pathway.

Mechanism and metabolic costs of HCN channel mediated control of conduction velocity

Our analysis revealed that the control of conduction velocity is solely mediated by changes in resting membrane potential. Isolated changes of membrane conductance and thus of the membrane time and length constant had no effect on conduction velocity (Fig. 10E). The speeding of conduction upon depolarization is consistent with a previously observed correlation between conduction velocity and the depolarization from the resting potential required to reach the firing threshold in motoneurons (Carp et al., 2003). On the other hand, Na^+ channels have a steep steady-state inactivation and are partially inactivated at the resting membrane potential in axons (Battefeld et al., 2014; Engel and Jonas, 2005; Rama et al., 2015). Depolarization could thus be expected to further inactivate Na^+ channels and decrease conduction velocity. However, our modelling results showed that increasing the membrane potential from –90 to –60 mV increased the conduction velocity despite significantly decreasing Na^+ channels availability (Fig. S2). Interestingly, these findings are in agreement with the nonlinear cable theory predicting that the difference between the resting membrane potential and the firing threshold is a critical parameter for action potential conduction velocity (see, e.g., Fig. 12.25 in Jack et al., 1983, for increasing velocity with increasing safety factor, i.e. decreasing excitation threshold V_B). Intuitively, the HCN channel mediated acceleration of conduction velocity can be understood as follows; in a more depolarized axon, Na_V mediated current influx in one axonal location will depolarize neighboring locations faster above the threshold. In our model, this effect outweighs the disadvantage of the increased steady-state inactivation of Na^+ channels up to a membrane potential of about –65 mV and a Na_V availability of 50%. The exact values, above which Na_V availability limits conduction velocity, critically depend on assumptions of the model, such as the voltage-dependence of inactivation and the

density of Na_V channel. Interestingly, Ca^{2+} entering through axonal voltage-gated Ca^{2+} channels (Bender et al., 2010) could interact with the cAMP pathway by activating or inhibiting different subtypes of adenylyl cyclase and phosphodiesterase (Bruce et al., 2003). Thereby, HCN could also serve a homeostatic role, by bringing the resting membrane potential closer to threshold and offsetting the inactivation of Na_V channels under conditions of high-frequency action potential firing.

Our findings indicate that the evolutionary design of HCN channels as a continuously open shunt for Na^+ influx causes significant metabolic costs. The high costs might appear surprising, because a metabolically cheaper way to depolarize the membrane would be the expression of less Na^+-K^+-ATPases resulting in a depolarized K^+ reversal potential (cf. V_m-*model* in Fig. 10). However, as discussed in the following paragraph, our finding that conduction velocity can be rapidly regulated via the cAMP-HCN pathway might provide a justification for the metabolic costs of axonal HCN channels.

Modulation of conduction velocity via the intracellular cAMP concentration

Using direct whole-cell recordings and immunogold EM from *en passant* boutons in cerebellar axons, we identified near exclusive HCN2 isoforms expression and a half-maximal shift of the activation of HCN2 channels at a cAMP concertation of 40 µM (Fig. 7D). Furthermore, our perforated patch-recordings from axonal compartments provide, to our knowledge, the first direct estimate of endogenous cAMP concentration in vertebrate central axons of 13 µM (Fig. 7D). This is higher compared to previous estimates of 50 nM in Aplysia sensory neurons (Bacskai et al., 1993; but see Greenberg et al., 1987) and 1 µM in cardiomyocytes (Börner et al., 2011). A recently reported low cAMP-sensitivity of protein kinase A (Koschinski and Zaccolo, 2017), a prototypical cAMP-regulated protein, also argues for high intracellular cAMP concentrations. On the other hand, our data do not rule out that such high cAMP concentration occur only in spatially restricted domains. The possibility for local cAMP signaling-compartments was recently observed in *Drosophila* axons (Maiellaro et al., 2016).

A high endogenous cAMP concentration and expression of the HCN2 isoform facilitates neuromodulators to bidirectionally and dynamically control conduction

velocity. Only norepinephrine increased the conduction velocity in cerebellar parallel fibers whereas the other neuromodulators reduced the velocity (Fig. 2), consistent with the expression of both G_i- and G_s-coupled receptors, respectively. Indeed, G_s-coupled receptors for serotonin, dopamine, and adenosine are expressed in the molecular layer of the cerebellum (see e.g. Geurts et al., 2002; Schweighofer et al., 2004). Interestingly, adenosine, which decreased the conduction velocity (Fig. 2), has been shown to be an endogenous sleep factor (Basheer et al., 2004; Porkka-Heiskanen et al., 1997). Moreover, serotonin, dopamine, and norepinephrine play important regulatory functions during sleep in, e.g., the cerebellum (Canto et al., 2017). Therefore, it is tempting to speculate that the cAMP-HCN pathway allows not only the increase in conduction velocity during arousal but also the decrease in velocity and saving of metabolic costs during periods of rest or sleep. The cAMP-HCN pathway in axons could thus contribute to the reduced energy consumption of the brain during sleep (Boyle et al., 1994; Townsend et al., 1973). It should be noted that the observed modulation of conduction velocity by neurotransmitters (Fig. 2) is consistent with a modulation via the cAMP-HCN pathway but other mechanisms, such as direct influences on voltage-dependent Na^+ (Yin et al., 2017), K^+ (Yang et al., 2013), and Ca^{2+} channels (Burke et al., 2018) could contribute to the modulation of conduction velocity.

Clinical relevance of axonal HCN channels

The function of HCN channels has been studied in human peripheral nerves using non-invasive threshold tracking techniques (Howells et al., 2016; Howells et al., 2012; Lorenz and Jones, 2014). Significant alterations of HCN channel expression and/or function have been described in pathologies such as stroke (Jankelowitz et al., 2007), porphyria (Lin et al., 2008), diabetic neuropathy (Horn et al., 1996), neuropathic pain (Chaplan et al., 2003), and inflammation (Momin and McNaughton, 2009) as well as a vertebrate model of demyelination (Fledrich et al., 2014). In some of these cases, the alterations are consistent with an activity-dependent modulation of HCN channels (Jankelowitz et al., 2007). Furthermore, HCN channel seem to be causally related to pain symptoms (Chaplan et al., 2003; Momin and McNaughton, 2009) and therapeutic blockade of HCN channels are also considered (Wickenden et al., 2009). Based on our

485 findings, HCN could also play a compensatory role in some diseases to restore
486 conduction velocity.

Methods

Cerebellar slice preparation

Cerebellar slices were prepared from P21-P46 C57BL/6 mice of either sex as reported previously (Delvendahl et al., 2015; Ritzau-Jost et al., 2014). In short, after anesthetization with isoflurane, mice were killed by rapid decapitation; the cerebellar vermis was quickly removed and placed in a slicing chamber filled with ice-cold extracellular solution (ACSF) containing (in mM): NaCl 125, KCl 2.5, $NaHCO_3$ 26, NaH_2PO_4 1.25, glucose 20, $CaCl_2$ 2, $MgCl_2$ 1 (pH adjusted to 7.3–7.4 with HCl). Parasagittal or horizontal slices were cut from the vermis of the cerebellum using a microtome with a vibrating blade (VT1200, Leica Biosystems, Nussloch, Germany), incubated at 35°C for approximately 30 minutes and subsequently stored at room temperature until use. For electrophysiological recordings, a slice was transferred into the recording chamber mounted on the stage of an upright Nikon microscope. The recording chamber was perfused with ACSF and the temperature in the center of the recording chamber was set to 35°C using a TC-324B perfusion heat controller (Warner Instruments, Hamden CT, USA).

Measuring conduction velocity in cerebellar parallel and mossy fibers

Compound action potentials were evoked by electrical stimulation using a bipolar platinum/iridium electrode (from Microprobes for Life Science, Gaithersburg MD, USA) placed either in the white matter or in the molecular layer (Fig. 1) of the cerebellum. For the extracellular recording of compound action potentials, two pipettes were filled with a 1M NaCl solution (tip resistance of 1–3 MΩ) and placed within the respective fiber bundle, and the voltage was measured in current clamp mode with an EPC10 amplifier (CC gain 10x). Compound action potentials were evoked at 0.5 Hz in parallel fibers and 1 Hz in the white matter. All recordings were performed in the presence of 10 µM NBQX to block synaptic potentials. The conduction velocity of PFs was measured at 35°C. Due to the higher conduction velocity in myelinated mossy fibers, action potentials evoked by white matter stimulation had to be recorded at room temperature to allow separation of the compound action potential from the stimulation artifact. To calculate the conduction velocity, we determined the delays of the peaks of the compound action potential component recorded with the proximal and distal

519 electrode. Compound action potentials from mossy fibers were analyzed offline using
520 the smoothing spline interpolation operation of Igor Pro to increase the signal to noise
521 ratio. Control recordings were performed interleaved with application of different drugs.
522 The conduction velocity experienced a small rundown over 20 minutes under control
523 conditions (Fig. 1 – 3).
524
525 *Measuring conduction velocity in the optic nerve*
526 Male wildtype mice of the C57BL6/N strain (P63 ± 4) were euthanized by decapitation.
527 After the brain was exposed, the optic nerves (ON) were separated from the retina at the
528 ocular cavity and both ONs were detached by cutting posterior to the optic chiasm. The
529 preparation was gently placed into an interface brain/tissue slice (BTS) perfusion
530 chamber (Harvard Apparatus) and continuously superfused with ACSF, bubbled with
531 carbogen (95% O_2, 5% CO_2) at 36.5 °C during the experiment (Trevisiol et al., 2017).
532 In case both nerves were used for experiments, the non-recorded ON was transferred in
533 a different incubation chamber (Leica HI 1210) that provided similar incubation
534 conditions to the recorded nerve while preventing exposure to ZD7288 and 8-Br-cAMP.
535 The temperature was maintained constant using a feedback-driven temperature
536 controller (model TC-10, NPI electronic) connected to a temperature probe (TS-100-S;
537 NPI electronic) inserted in the BTS incubation chamber near the nerve. Each ON was
538 detached from the optic chiasm and individually placed into the suction electrodes for
539 stimulation/recording. The stimulation's direction of the ON was maintained constant
540 (orthodromic) throughout the experiments by inserting the proximal (retinal) end of the
541 nerve into the stimulation electrode as illustrated in Fig. 1I. The stimulating electrode
542 was connected to a battery (Stimulus Isolator A385; WPI) that delivered a
543 supramaximal stimulus to the nerve. The voltage was pre-amplified 500 times and fed
544 to the AD ports of the EPC9 or acquired directly via the EPC9 headstage (HEKA
545 Elektronik, Lambrecht/Pfalz). The reference channel was obtained from an ACSF-filled
546 glass capillary next to the recording suction electrode, in contact with the bathing
547 ACSF. Initial equilibration of the ONs was performed at 0.1 Hz stimulation, until the
548 recorded compound action potentials showed a steady shape (typically around 45-60
549 min from preparation). 5 nerves from 4 animals and 4 nerves from 4 animals were used
550 for ZD7288 and 8-Br-cAMP treatment, respectively. Compound action potentials were

analyzed as described above using the smoothing spline interpolation operation of Igor Pro to increase the signal to noise ratio.

Recordings from cMFBs

cMFBs were visualized as previously described (Delvendahl et al., 2015; Ritzau-Jost et al., 2014) with infrared differential interference contrast (DIC) optics using a FN-1 microscope from Nikon with a 100x objective (NA 1.1) or infrared oblique illumination optics using a Femto-2D two-photon microscope (Femtonics, Budapest) with a 60x Olympus (NA 1.0) objective. The passive properties of the cMFB were determined as previously described (Hallermann et al., 2003) and revealed similar values for a two-compartment model (data not shown) as previously described for cMFBs (Ritzau-Jost et al., 2014), indicating that we indeed recorded from cMFBs. Furthermore, the access resistance was on average 16.9 ± 0.9 MΩ (n = 53 cMFBs), indicating optimal voltage clamp conditions.

To elicit traveling action potentials by axonal stimulation with a second pipette (Fig. 5A), whole-cell recordings from cMFBs were performed with 50 µM green fluorescent dye Atto488 in the intracellular solution to visualize single mossy fiber axons. The additional stimulation pipettes filled with ACSF and 50 µM of the red-fluorescent dye Atto594 had the same opening diameter as patch pipettes and were positioned close to the axon and approximately 100 µm apart from the patched terminal. Stimulation pulses with durations of 100 µs were delivered by a voltage-stimulator (ISO-Pulser ISOP1, AD-Elektronik, Buchenbach, Germany). The stimulation intensity (1-30 V) was adjusted to ensure failure-free initiation of action potentials at 1 Hz (~1.5 time the firing threshold). High-frequency trains of action potentials were evoked at 100, 200 333, 500, 750, 1000, 1111 and 1666 Hz. Amplitudes were measured from peak to baseline. The duration was determined at half-maximal amplitude and is referred to as half-width. Action potentials were treated as failures if the peak did not exceed –40 mV.

Recordings were performed with an EPC10/2 patch-clamp amplifier, operated by the corresponding software PatchMaster (HEKA Elektronik), running on a personal computer. Recording electrodes were pulled from borosilicate glass capillaries (inner

583 diameter 1.16 mm, outer diameter 2 mm) by a microelectrode puller (DMZ-Universal
584 Puller, Zeitz Instruments, Augsburg). Pipettes used for patch-clamp recordings had
585 open-tip resistances of 5–12 MΩ. The intracellular presynaptic patch pipette contained
586 (in mM): K-gluconate 150, MgATP 3, NaGTP 0.3, NaCl 10, HEPES 10 and EGTA
587 0.05. The apparent input resistance of cMFBs was estimated by linear regression of the
588 steady-state voltage in response to 300 ms hyperpolarizing current pulses of increasing
589 amplitude (–5 to –20 pA), while the apparent membrane time constant was determined
590 by fitting the voltage response to a -10 pA hyperpolarizing pulse with a mono-
591 exponential function.
592
593 I_h activation curves determined from analysis of normalized tail current were fitted with
594 a Boltzmann function:

595 $$\frac{I}{I_{max}} = \frac{1}{1 + e^{\frac{V - V_{½}}{k}}}$$

596 where V is the holding potential, $V_{½}$ is the voltage of half-maximal activation and k the
597 slope factor. The reversal potential of I_h was calculated from leak-subtracted currents
598 evoked by 10 ms long voltage ramps extending across the activation range of I_h (Cuttle
599 et al., 2001). Three I-V relationships recorded at holding potentials of –80, –110 and –
600 140 mV were linearly extrapolated and the reversal potential was measured from the
601 point of intersection of the three linear fits.
602
603 *Perforated patch recordings*
604 For perforated-patch recordings from cMFBs, a nystatin stock solution was prepared by
605 dissolving the pore-forming antimycotic in DMSO (25 mg/ml). Immediately before the
606 experiments, the nystatin-stock was added to the intracellular solution at a final
607 concentration of 50 µg/ml. In order to monitor the integrity of the perforated membrane
608 patch, the green-fluorescent dye Atto 488 (from Atto-Tec, Siegen,
609 Germany) was added at a concentration of 50 µM. Since nystatin is known to impair the
610 formation of the GΩ seal, the initial ~500 µm of the pipette tip was filled with a
611 perforating agent-free internal solution before back-filling the pipette shaft with the
612 perforating agent-containing solution. After establishing a GΩ seal, the holding
613 potential was set to –70 mV and the access resistance (R_a) was continuously monitored

by applying 10 ms long depolarizing pulses to –60 mV at 1 Hz. Recording the voltage-dependent activation of I_h was started after R_a dropped below 150 MΩ. Because the perforated membrane patch ruptured spontaneously with R_a < 50 MΩ, the access resistance was not comparable to standard whole-cell recordings. To exclude the possibility that the right-shift of the I_h activation curve in the perforated configuration (Fig. 8C) was caused by the comparatively higher R_a, the voltage-dependent activation of I_h was measured under normal whole-cell patch-clamp conditions, using pipettes with small openings resulting in high access resistances (R_a = 119 ± 12 MΩ). However, in these recordings, the midpoint of I_h activation (–105.5 ± 1.4 mV; n = 8) had a tendency to be left-shifted compared with regular whole-cell recordings with standard patch pipettes ($R_a \approx$ 30-60 MΩ; $V_{½}$ = –103.3 ± 0.8 mV; n = 36; $P_{T\text{-}Test}$ = 0.13). The left-shift of the I_h activation curve measured with high access resistances indicates that the right-shift measured with perforated patch recordings might be underestimated due to the higher R_a, which would result in an even higher estimate of the endogenous cAMP concentration (Fig. 7D).

Analysis of ZD sensitivity of Na^+ currents

Sodium currents (Fig. S1) were isolated using a modified ACSF containing (in mM): NaCl 105, KCl 2.5, $NaHCO_3$ 25, NaH_2PO_4 1.25, glucose 20, $CaCl_2$ 2, $MgCl_2$ 1, TEA 20, 4-AP 5 and $CdCl_2$ 0.2. To avoid underestimating the true size of the presynaptic Na^+ currents due to the voltage-drop through the access resistance, we blocked a portion of the Na^+ current with 30 nM TTX. Na^+ currents were elicited from a holding potential of –80 mV by a 3 ms long depolarization to 0 mV. Peak amplitudes and half-durations of Na^+ currents were measured from leak-subtracted traces.

Immunoelectron microscopy

Preembedding immunogold labeling was performed as described (Notomi and Shigemoto, 2004). Briefly, adult C57Bl/6 mice were anesthetized with sodium pentobarbital (50 mg/kg, i.p.) and perfused transcardially with a fixative containing 4% formaldehyde, 0.05% glutaraldehyde and 15% of a saturated picric acid in 0.1 M phosphate buffer (PB, pH 7.4). Parasagittal sections through the cerebellum were cut at 50 µm, cryoprotected with 30% sucrose, flash frozen on liquid nitrogen and rapidly

thawed. Sections were blocked in 10% normal goat serum and 2% bovine serum albumin (BSA) in Tris-buffered saline (TBS) for 2 h at room temperature, incubated in TBS containing 2% BSA and either guinea pig anti-HCN1 or anti-HCN2 antibody (1 µg/ml, Notomi and Shigemoto, 2004) for 48 h at 4°C, and finally reacted with nanogold-conjugated secondary antibody (Nanoprobes, 1:100) for 24 h at 4°C. Nanogold particles were amplified with HQ Silver Enhancement kit (Nanoprobes) for 8 min. Sections were then treated in 0.5% osmium tetroxide in PB for 40 min, 1% aqueous uranyl acetate for 30 min at room temperature, dehydrated, and flat embedded in Durcopan resin (Sigma-Aldrich). Ultrathin sections were cut at 70 nm and observed by a transmission electron microscope (Tecnai 12, FEI, Oregon). Sequential images were recorded from the granule cell layer within a few microns from the surface of ultrathin sections at X26,500 using a CCD camera (VELETA, Olympus). For the reconstruction of a half mossy fiber bouton, 36 serial ultrathin sections were used. Sequential images were aligned and stacked using TrakEM2 program (Cardona et al., 2012). For the measurement of density of immunogold particles for HCN2 on this reconstructed profile, 1260 immunogold particles were counted on the mossy fiber bouton membrane area (73.7 μm^2), giving a density of 17.1 particles/μm^2. Immunogold particles within 30 nm from the bouton membranes were included in the analysis based on the possible distance of the immunogold particle from the epitope (Matsubara et al., 1996). The density of non-specific labeling was estimated using nuclear membrane of a granule cell located adjacent to the reconstructed mossy fiber bouton. We found 40 immunogold particles on the nuclear membrane area of 60.5 μm^2 giving a density of 0.66 particles/μm^2, which was 3.9% of the HCN2 labeling density on the mossy fiber bouton.

Hodgkin-Huxley model of axonal HCN channels

Because we did not intend to implement the cAMP dependence of HCN channels explicitly (Hummert et al., 2018), we created two separate models for 0 and 1 mM intracellular cAMP, which were based on a previously described Hodgkin-Huxley model (Kole et al., 2006) with one activation gate and no inactivation (Hodgkin and Huxley, 1952). In short, the activation gate was described by

$$\frac{dm}{dt} = \alpha_m(1 - m) - \beta_m m$$

678 with

679 $$\alpha_m(V) = A\, e^{\frac{-(V_m - V_{1/2})}{V_\alpha}}$$

680 and

681 $$\beta_m(V) = A\, e^{\frac{(V_m - V_{1/2})}{V_\beta}}$$

682

683 The four free parameters, A, $V_{1/2}$, V_α, and V_β were determined by simultaneously fitting
684 $\alpha_m/(\alpha_m + \beta_m)$ to the steady-state activation curve (see Fig. 7B) and $1/(\alpha_m + \beta_m)$ to the
685 voltage dependence of the time constant of I_h activation and deactivation (Fig. 9B). The
686 sum of squared errors was minimized using the FindMinimum routine of Mathematica
687 (version 10; Wolfram Research, Champaign, IL), with the time constants of activation
688 and deactivation weighed with the inverse of the square of the maximum value in each
689 of the three datasets (time constant of activation, time constant of activation, steady-
690 state activation curve). The resulting parameters for 0 mM cAMP were A = 6.907 ms^{-1},
691 $V_{1/2}$ = –102.1 mV, V_α = 18.71 mV, and V_β = 21.73 mV. To confirm that the global
692 minimum was reached, the best-fit parameters were shown to be independent of the
693 starting values within a plausible range. The 68% confidence interval was calculated as
694 the square roots of the diagonals of the inverse of the Hessian matrix (Press et al., 2002)
695 resulting in ±2.71 ms^{-1}, ±16.5 mV, ±17.5 mV, and ±24.3 mV for A, $V_{1/2}$, V_α, and V_β,
696 respectively. We also generated a model for the corresponding data obtained with 1 mM
697 cAMP in the intracellular solution (cf. Fig 5B), resulting in A = 7.570 ms^{-1}, $V_{1/2}$ = –
698 87.31 mV, V_α = 31.46 mV, and V_β = 10.84 mV.

699

700 *NEURON model of cMFB*

701 The model of the cMFB consisted of connected cylindrical compartments representing
702 15 boutons (length and a diameter 8 µm) and 15 myelinated axonal compartments
703 (length 35 µm and a diameter 0.8 µm; cf. Palay and Chan-Palay, 1974; Fig. 10A). In
704 addition, at one side of this chain a long cylinder was added presenting the axon in the
705 white matter (length 150 µm and a diameter 1.2 µm). The specific membrane resistance
706 was 0.9 µF/cm^2 (Gentet et al., 2000) and the cytoplasmatic resistivity was 120 Ω/cm
707 (Hallermann et al., 2003). The specific membrane resistance of the axonal
708 compartments was reduced by a factor of 10 representing myelination.

709

710 The active membrane conductances were similar to Ritzau-Jost et al. (2014) and were
711 adjusted to reproduce the action potential duration and maximal firing frequency as well
712 as the data shown in Figs. 10B-D. Namely, an axonal Na^+ channel (Schmidt-Hieber and
713 Bischofberger, 2010) and K^+ channel NMODL model (Hallermann et al., 2012) was
714 added with a density of 2000 and 1000 pS/µm^2 in the boutons and 0 and 0 pS/µm^2 in the
715 axonal compartments, respectively. The Na^+ and K^+ reversal potentials were 55 and –97
716 mV, respectively. To investigate ATP consumption, separate Na^+ and K^+ leak channel
717 models were added, with a conductance of 0.0138 and 0.18 pS/µm^2, respectively, in the
718 bouton compartments. In the axonal compartments, both conductances were reduced by
719 a factor of 10. The above described Hodgkin-Huxley model of axonal HCN channels for
720 either 0 or 1 mM intracellular cAMP was added with a density of g_{HCN} = 0.3 and 0.03
721 pS/µm^2 for the bouton and axonal compartments, respectively, to reproduce the data
722 shown in Fig. 10B-D. To investigate ATP consumption, the conductance was separated
723 in a Na^+ and a K^+ conductance according to $g_{HCN(Na)} = (1 - ratio_{K/Na})\ g_{HCN}$ and $g_{HCN(K)} =$
724 $ratio_{K/Na}\ g_{HCN}$, where $ratio_{K/Na} = (e_{Na} + e_{HCN})/(e_{Na} - e_K)$, where e_{Na} and e_K are the Na^+
725 and K^+ reversal potential as described above and e_{HCN} is the reversal potential of I_h
726 measured as –23.3 mV (cf. Fig. 9C). Assuming a single channel conductance of 1.7 pS
727 for HCN2 channels (Thon et al.), this conductance corresponds to a density of 0.18
728 HCN channels/µm^2, which is much lower than the estimate from preembedding
729 immunogold labeling (22 particles/µm^2; Fig. 8). However, the optimal density of the
730 model critically depends on the geometry of the structure, which was not obtained from
731 the recorded boutons. To obtain the required structural information including the
732 fenestration of the cMFB (cf. Fig. 8) and the level of myelination, electron microscopic
733 reconstructions of large volumes of the recorded cMFB and the entire axon would be
734 needed. When we used a g_{HCN}, as determined with preembedding immunogold labeling
735 in our model, the model also predicted that I_h critically effects conduction velocity and
736 that the depolarization is the main reason for the velocity to change. In general, these
737 two conclusions of the model were very insensitive to the specific parameters of the
738 model and were, e.g., also obtained with additional interleaved cylindrical
739 compartments with high Na^+ and K^+ channel density representing nodes of Ranvier or
740 with a long cylindrical compartment with homogenous channel densities representing

an unmyelinated axon. This further supports our finding that HCN channels accelerate conduction velocity independent of the exact parameters of the axon and the degree of myelination (cf. Fig. 1).

Starting from the model that reproduced the control data, the following four additional models were generated: (1) To simulate ZD application, the HCN HH model was removed. (2) To simulate 8-br-cAMP application, parameters of the HCN HH model were exchanged with the parameters obtained from the experiments with 1 mM cAMP as described in the section above. (3) To simulate only the depolarization by HCN channels (*V_m-model*), the HCN HH channel model was removed and the K^+ reversal potential was increased from –97 mV to –90 mV. (4) To simulate only the increase in membrane conductance by HCN channels (*R_m-model*), the reversal potential of the HCN HH model was decreased from –23.3 mV to –85.5 mV and the density was increased from 0.3 pS/µm^2 to 1 pS/µm^2.

All simulations were run with a simulation time interval (*dt*) of 0.2 ms, preceded by a simulation of 1 s with a *dt* of 5 ms to allow equilibration of all conductances. Conduction velocity was calculated from the peak of the action potentials in different boutons of the model. The apparent input resistance was calculated identical to the experimental recordings, i.e. from the voltage after 300 ms of a –10 pA current injection. Mathematica was used to execute the NEURON simulations and to visualize and analyze the automatically imported NEURON results.

Statistics

Statistical analysis was performed using built-in functions of Igor Pro (Wavemetrics, Lake Oswego, OR). The suffix of the P values provided in the legends and the main test indicate the used statistical test. Results were considered significant with $P < 0.05$.

Code

The NEURON and Mathematica scripts to reproduce the model results will be available at: https://github.com/HallermannLab/2018_eLife_HCN.

Acknowledgement

We would like to thank Klaus Nave and the department of Neurogenetics at the Max Planck Institute of Experimental Medicine for scientific support. This work was supported by the German Research Foundation (HA 6386/4-1) to S.H.

Figures and Legends

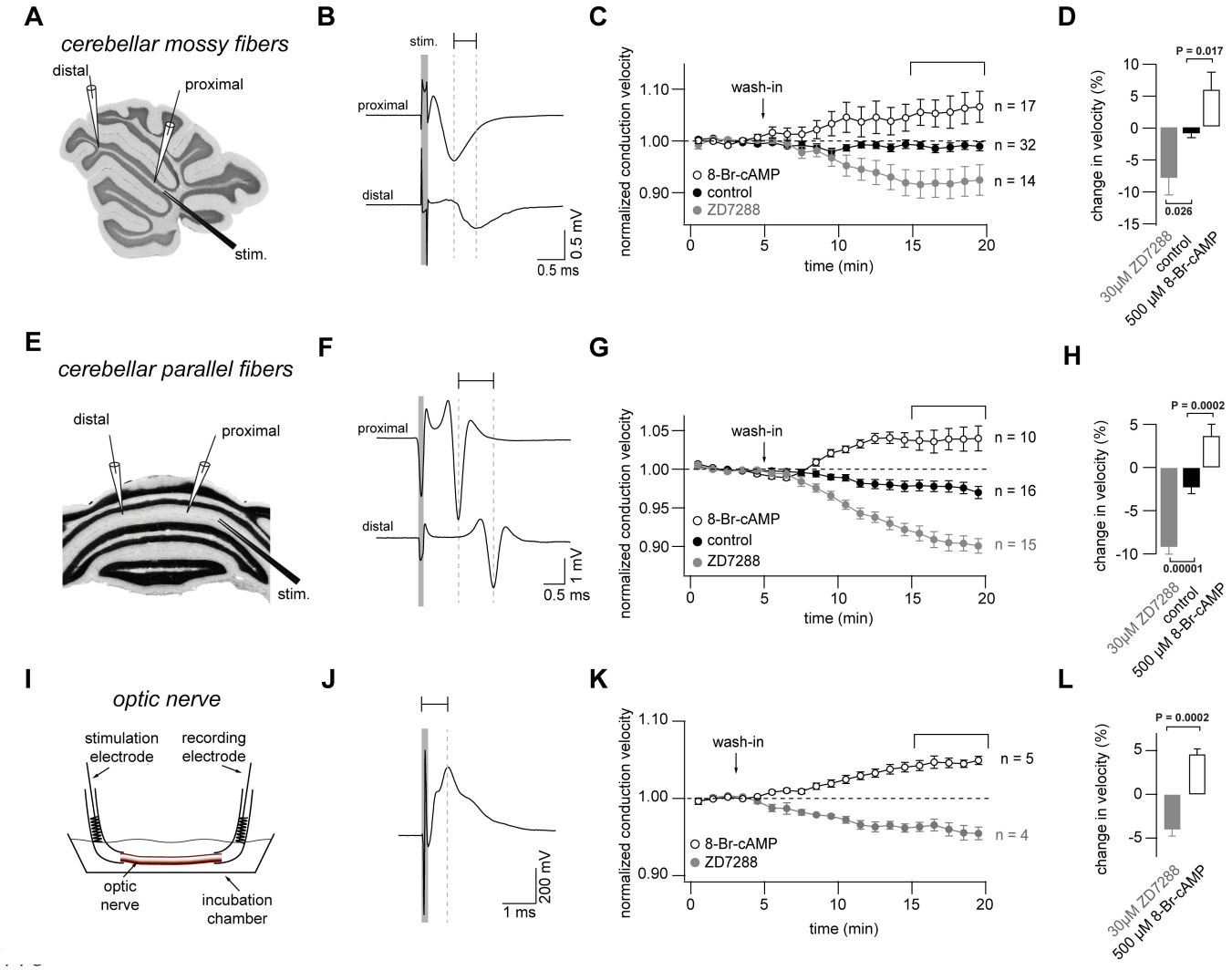

Figure 1. Bidirectional modulation of conduction velocity

(A) Recording configuration of conduction velocity in mossy fibers using a bipolar tungsten stimulation electrode (stim.) and two glass electrodes filled with 1M NaCl solution.

(B) Example of compound action potentials recorded with two electrodes positioned with different distance in relation to the stimulation electrode. Stimulation was 100 µs as indicated by the grey bar. Each trace is an average of 50 individual compound action potentials recorded at 1Hz.

(C) Average normalized mossy fiber conduction velocity, during bath application ZD7288 (30 µM) or 8-Br-cAMP (500 µM) at t = 5 min.

(D) Average relative change in mossy fiber conduction velocity after application of ZD7288 or 8-Br-cAMP measured 10 to 15 minutes after wash-in (bracket in C). $P_{ANOVA} = 0.00015$. $P_{Kruskal\text{-}Wallis} = 0.00044$. The individual P values of the Dunnett test for multiple comparisons with control are indicated.

(E) Schematic illustration of the experimental configuration used to record from cerebellar parallel fibers.

(F) Examples of compound action potentials recorded from parallel fibers, as in panel B.

(G) Normalized conduction velocity in parallel fibers, as in panel C.

(H) Average relative changes in parallel fiber, as in panel D. $P_{ANOVA} = 10^{-9}$. $P_{Kruskal\text{-}Wallis} = 10^{-8}$. The individual P values of the Dunnett test for multiple comparisons with control are indicated.

(I) Schematic of the experimental configuration used to record from optic nerve.

(J) Examples of compound action potentials recorded from optic nerve, as in panel B.

(K) Normalized conduction velocity in optic nerve, as in panel C.

(L) Average relative changes in optic nerve, as in panel D. $P_{T\text{-}Test} = 0.0002$. $P_{Wilcoxon\text{-}Mann\text{-}Whitney\text{-}Test} = 0.004$.

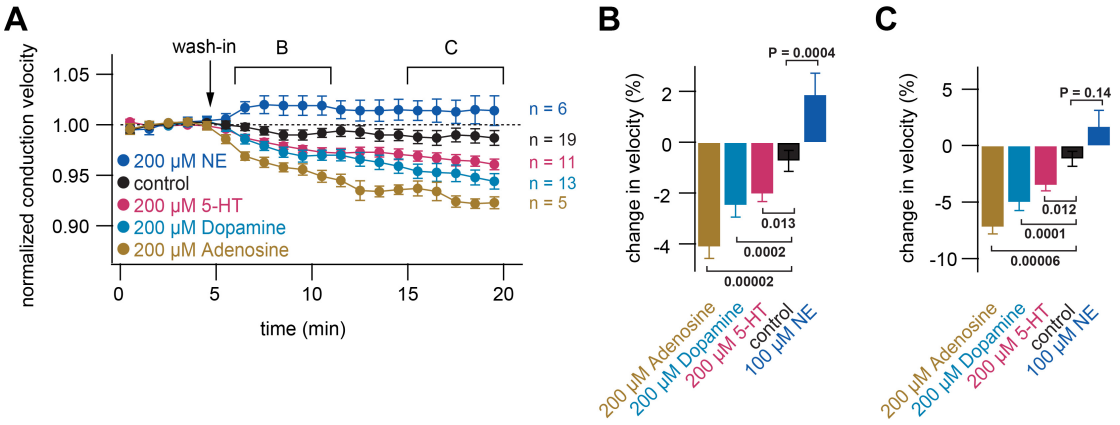

807

808

809 **Figure 2. Neuromodulators differentially regulate conduction velocity**

810 (A) Average normalized conduction velocity in cerebellar parallel fibers during wash-in
811 at t = 5 min of various neuromodulators known to act via cAMP-dependent
812 pathways.

813 (B) Average relative change in conduction velocity after application of the
814 neuromodulators measured from 1 to 6 minutes after wash-in (bracket marked B in
815 panel A). $P_{ANOVA} = 9*10^{-10}$. $P_{Kruskal\text{-}Wallis} = 3*10^{-8}$. The individual P values of the
816 Dunnett test for multiple comparisons with control are indicated.

817 **(C)** Average relative change in conduction velocity after application of the
818 neuromodulators measured 10 to 15 minutes after wash-in (bracket marked C in
819 panel A). $P_{ANOVA} = 3*10^{-7}$. $P_{Kruskal\text{-}Wallis} = 3*10^{-7}$. The individual P values of the
820 Dunnett test for multiple comparisons with control are indicated.

821

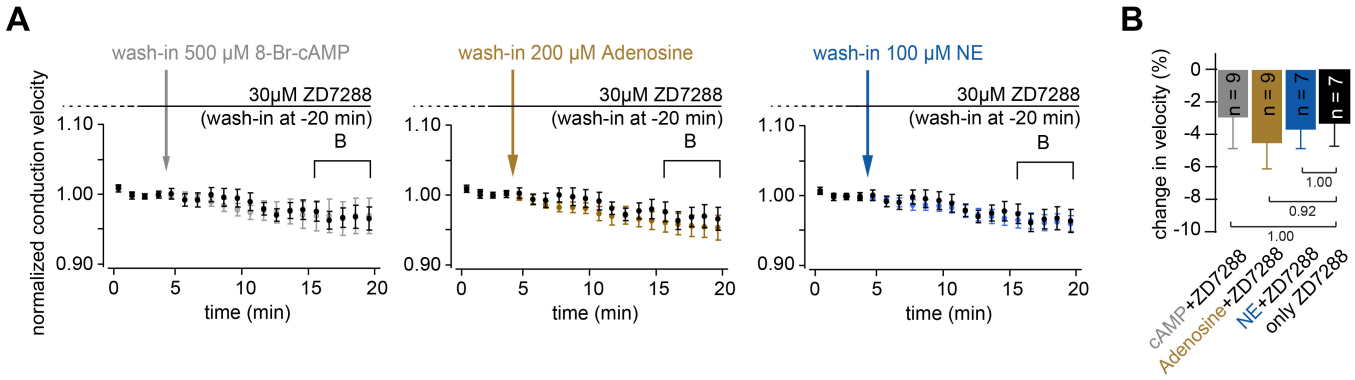

Figure 3. Neuromodulation of conduction velocity is mediated by HCN channels

(A) Average normalized conduction velocity in parallel fibers. Wash-in of 30 µM ZD7288 20 minutes before the start of the recording. The substance remained in the solution during recording to ensure continuous block HCN channels. At t = 5 min, 8-Br-cAMP, Adenosine or NE was added to the solution.

(B) Average relative change in conduction velocity after application of the neuromodulators measured 10 to 15 minutes after wash-in (bracket marked B in panel A). P_{ANOVA} = 0.91. $P_{Kruskal\text{-}Wallis}$ = 0.77. The individual P values of the Dunnett test for multiple comparisons with control are indicated.

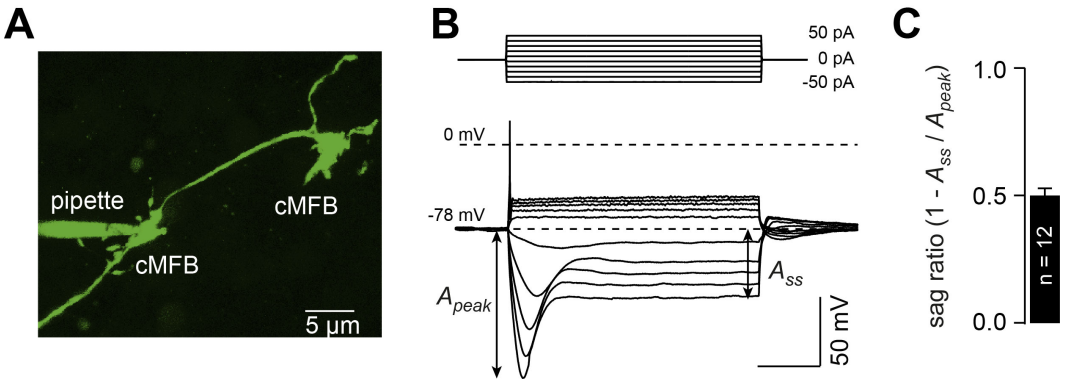

834

835

836 **Figure 4. Cerebellar mossy fiber terminals have a prominent voltage sag**

837 (A) Two-photon microscopic image of a whole-cell patch-clamp recording from a
838 cMFB (green) filled with the fluorescence dye Atto 488 in an acute cerebellar brain
839 slice of an adult 39-days old C57/Bl6 mouse (maximal projection of stack of
840 images).

841 (B) Characteristic response of a cMFB to current injection: Depolarizing pulses evoked
842 a single action potential while hyperpolarizing pulses evoked a strong
843 hyperpolarization with a sag.

844 (C) Average sag ratio of 12 cMFB recordings.

845

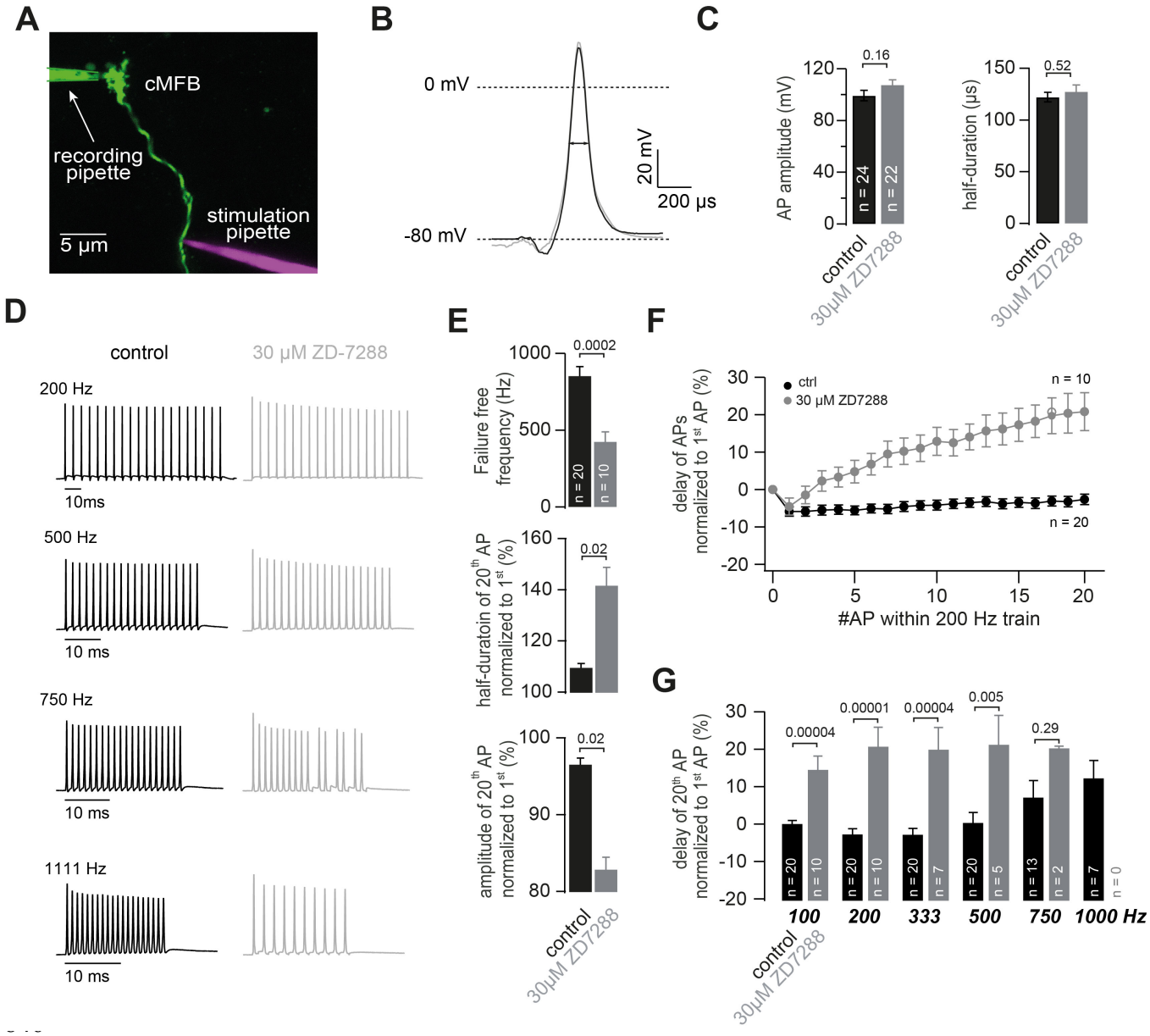

Figure 5. HCN channels support high frequency action potential firing

(A) Two-photon microscopic image of a whole-cell patch-clamp recording from a cMFB (green) filled with the fluorescence dye Atto 488 in an acute cerebellar brain slice of an adult 43-days old mouse (maximal projection of stack of images). Targeted axonal stimulation was performed by adding a red dye Atto 594 to the solution of the stimulation pipette.

(B) Grand average of action potentials evoked at 1 Hz under control conditions (black) and in the presence of ZD7288 (grey).

(C) Average action potential amplitude (measured from resting to peak) and half-duration $P_{T\text{-}Test}$ = 0.16 and 0.51, for amplitude and resting respectively.

(D) ZD7288 effects the ability of cerebellar mossy fibers to fire high frequency action potentials: Examples of two different cMFBs stimulated at frequencies between 200 Hz and 1111 Hz under control conditions (*left, black*) or in the presence of 30 µM ZD7288 (*right, grey*).

(E) cMFBs treated with ZD7288 showed an on average lower maximal failure-free firing frequency. In addition, amplitude reduction and action potential broadening during 200-Hz trains of action potentials in ZD7288 treated axons were more pronounced than under control conditions.

(F) Average delay between the peak of the action potentials (AP) and the stimulation during 200 Hz trains of 20 action potentials normalized to the delay of the first action potential for control conditions (*black*) and in the presence of 30 µM ZD7288 (*grey*).

(G) Average delay of the 20^{th} normalized to the delay of the 1^{st} action potential during trains of 20 action potentials at frequencies ranging from 100 to 1000 Hz. The provided P-values based on simple t-test are mostly much smaller than the Bonferroni-corrected significance left of 0.05/6 = 0.008, indicating a highly significant slowing of the conduction velocity during high-frequency trains.

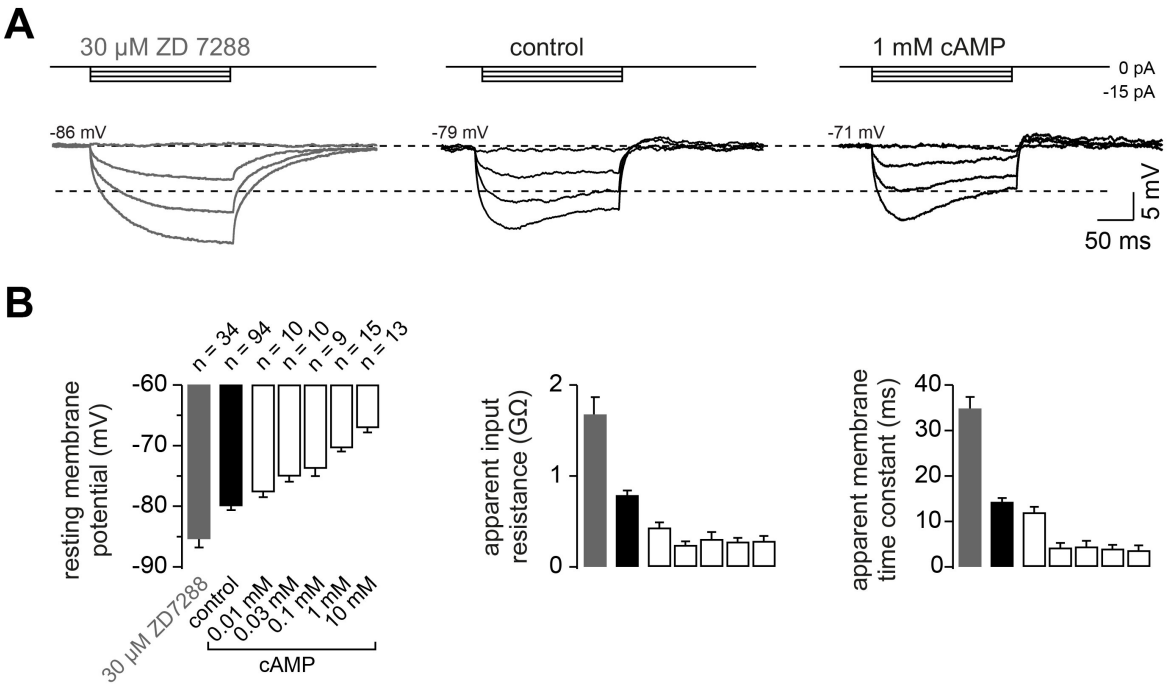

Figure 6. The passive membrane properties of cMFBs are HCN and cAMP-dependent

(A) Example voltage response of cMFBs to small hyperpolarizing current steps. Application of 30 µM ZD7288 eliminated the I_h-mediated voltage sag (left). Adding 1 mM cAMP to the intracellular path-clamp solution (right) reduced the input resistance as seen by the reduced steady-state voltage response (dashed lines).

(B) Average resting membrane potential (left), apparent input resistance (middle), and apparent membrane time constant (right) upon application of 30µM ZD7288 or different concentrations of cAMP. For all three parameters, P_{ANOVA} and $P_{Kruskal\text{-}Wallis}$ are $< 10^{-10}$ and the Dunnett test for multiple comparisons with control indicates, e.g., $P < 0.0001$ for control vs. ZD and $P < 0.001$ for control vs. 1 mM cAMP.

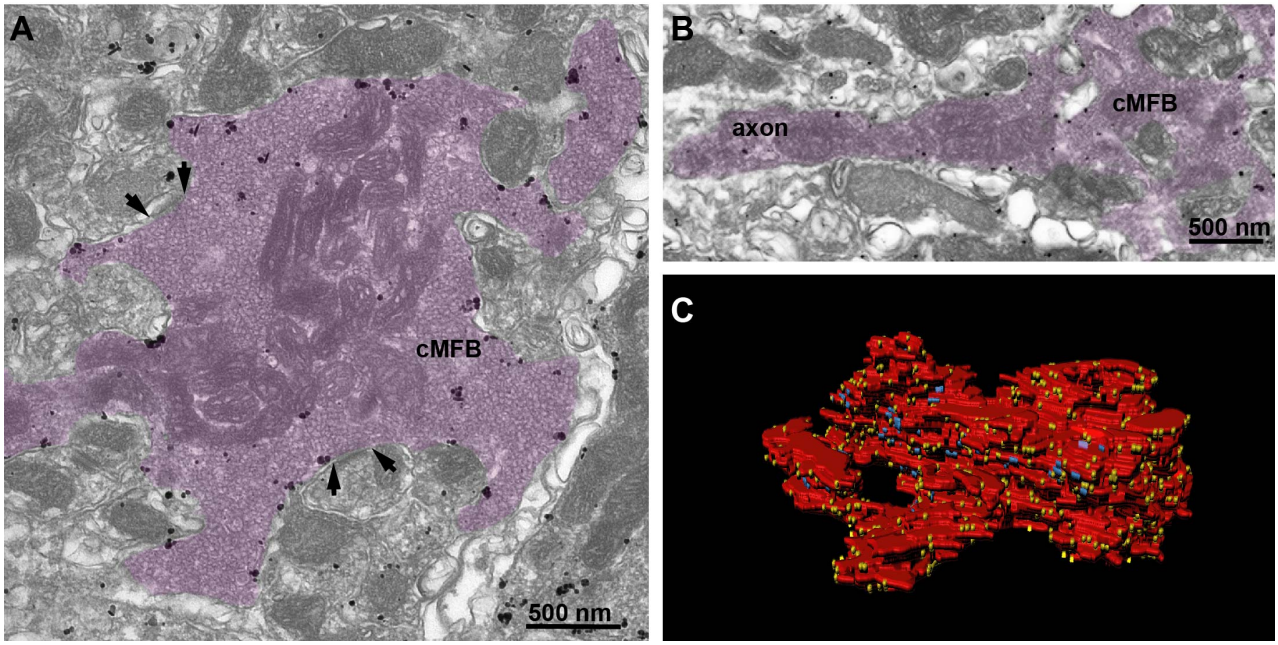

Figure 7. HCN2 is uniformly distributed in mossy fiber axons and boutons

(A) Electron microscopic image showing a cMFB (magenta) labeled for HCN2. Many particles are diffusely distributed along the plasma membrane of the cMFB, some of them being clustered. Arrows mark synapses between the cMFB and dendrites of adjacent GCs.

(B) Another cMFB, showing similar labeling density for HCN2 in a proximal part of the mossy fiber axon.

(C) Reconstructed cMFB (red) with identified synapses (blue) and HCN2 labeled with gold particles (yellow).

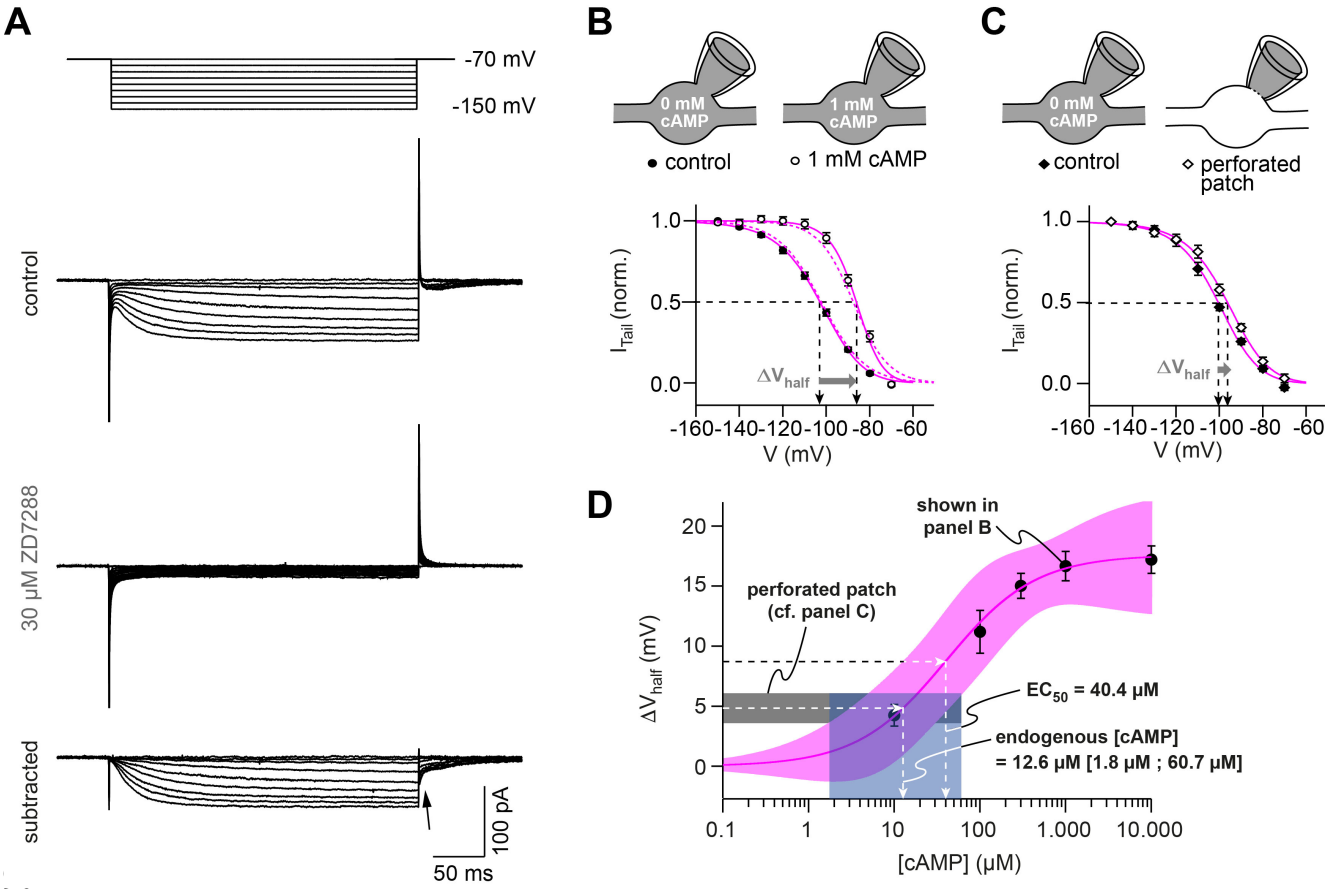

Figure 8. HCN channels in cMFB are strongly modulated by cAMP

(A) Example currents elicited hyperpolarizing voltage steps (–70 mV and then stepped to conditioning pulses between –80 mV and –150 mV). *Top*, the control current, *middle,* remaining transients in the presence of 30 µM ZD7288 and, *bottom*, the subtracted currents. The ZD7288-sensitive current is slowly activating, non-inactivating and shows inward tail currents (arrow).

(B) Activation curve of I_h determined as the normalized tail current of ZD7288 sensitive currents obtained after the end of the conditioning voltage pulse (*arrow in A*) plotted versus corresponding voltage pulse with 0 mM cAMP (filled circles, n = 36) and 1 mM cAMP (open circles, n = 15) in the intracellular solution. Sigmoidal fits (continues magenta lines), yielding midpoints of I_h activation ($V_{½}$, arrows). The steady-state activation curves produced by the Hodgkin-Huxley models (dotted magenta line) are superimposed. *Inset on top*: Illustration of the whole-cell recording configuration with 0 and 1 mM cAMP in the intracellular solution.

(C) Activation curve obtained with perforated-patch recordings show a shift in the I_h activation curve by 4.8 ± 1.2 mV compared to recordings from the same cell after rupture of the perforated membrane patch (n = 10). *Inset on top*: Illustration of the whole-cell recording configuration with 0 mM cAMP in the intracellular solution and in the perforated patch configuration, where the intracellular cAMP concentration is unperturbed.

(D) Shift in I_h $V_{½}$ versus the corresponding cAMP concentration (mean ± SEM). Fitting the data with a Hill equation revealed an EC_{50} of 40.4 µM. Superposition of the 68% confidence band of the fit (straight line and light magenta area) with the average voltage shift observed in perforated patch recordings (4.8 ± 1.2 mV, n = 10, dotted black line and grey area) results in an estimated cAMP-concentration in the non-perturbed presynaptic boutons of 12.6 µM with a range of 1.8 to 60.7 µM cAMP (dotted line and light blue area).

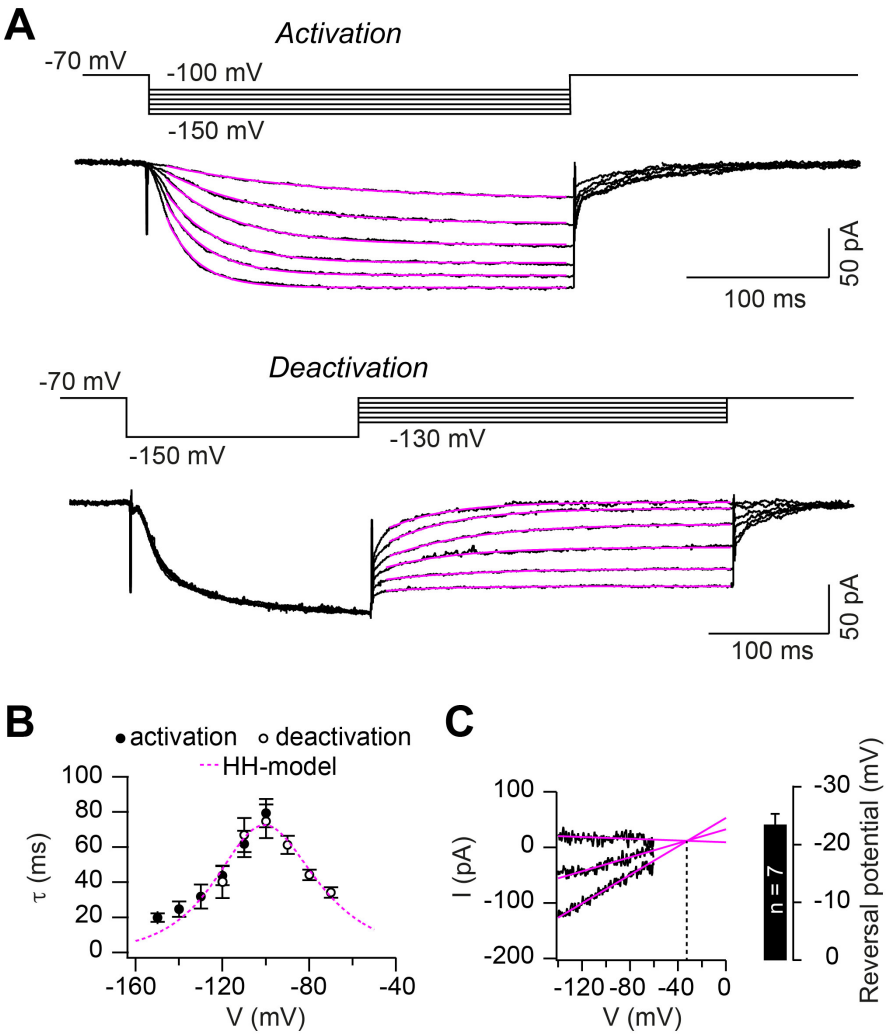

Figure 9. Hodgkin-Huxley model describing HCN2 channel gating

(A) Example of ZD7288 sensitive currents (black) elicited by the illustrated activation (*top*) and deactivation voltage protocols (*bottom*) superimposed with a mono-exponential fits (magenta).

(B) Average time constants of activation (filled circles) and deactivation (open circles; mean ± SEM). The dotted blue line represents the prediction of I_h activation and deactivation time constant based on the Hodgkin-Huxley model.

(C) Example of linear extrapolation (magenta lines) of leak subtracted currents evoked by fast (10 ms) voltage ramps generated from a range of holding potentials that extended across the activation range of I_h. The reversal potential was found to be –36 mV in this example. *Inset:* average reversal potential of 7 independent experiments.

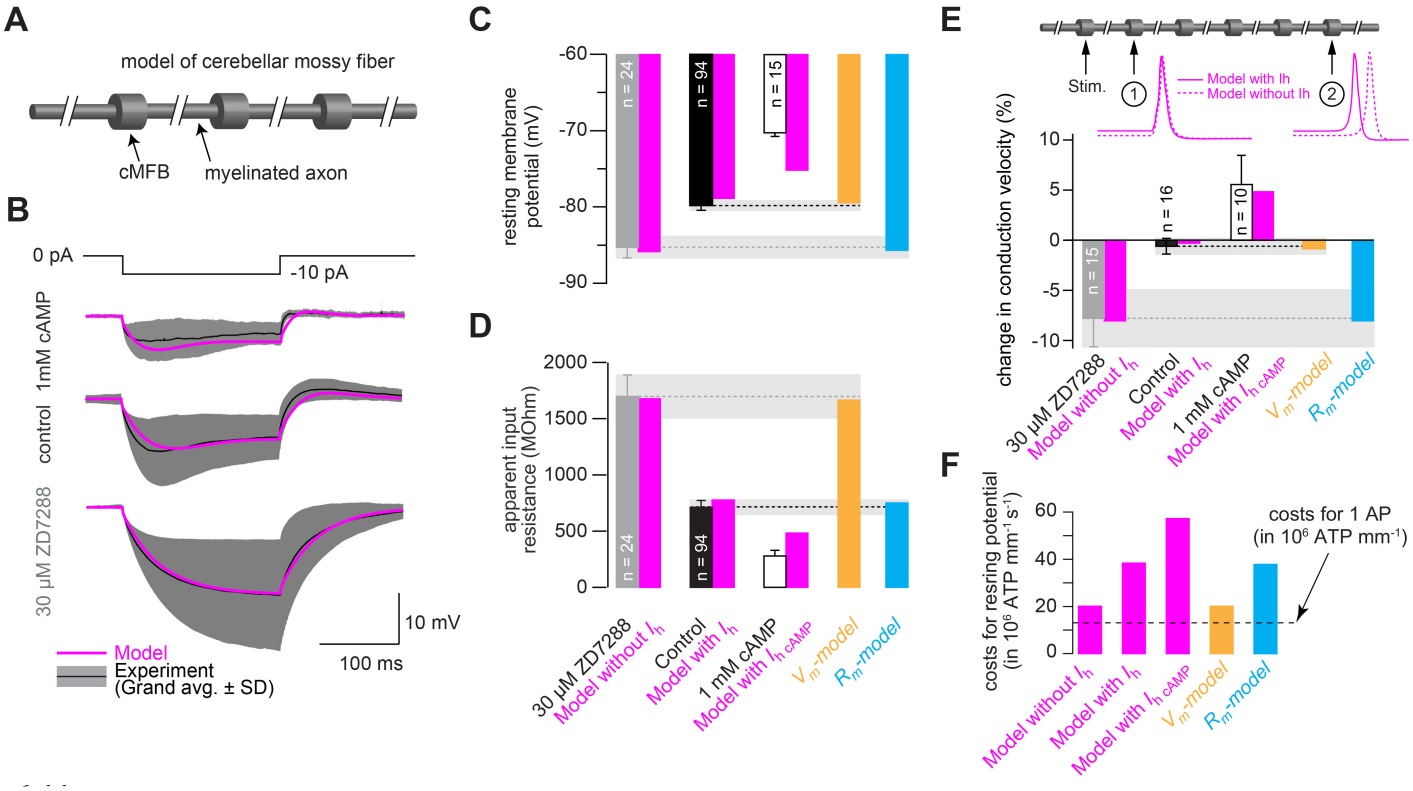

945 **Figure 10. Mechanism of conduction velocity-control and metabolic costs of HCN**
946 **channels**

947 (A) Illustration of cerebellar mossy fiber model consisting of 15 connected cylindrical
948 compartments representing cMFBs and the myelinated axon.

949 (B) Grand average voltage response (black) and standard deviation (grey area) of
950 cMFBs in response to a –10 pA hyperpolarizing current pulse with 1mM cAMP
951 included in the patch pipette (top), under control conditions (middle) or treated with
952 ZD7288 (bottom), superimposed with the predicted voltage response from the
953 model (magenta).

954 (C) Average resting membrane potential of cMFBs measured under control conditions
955 (black), with I_h blocked by ZD7288 (gray), or enhanced by 1 mM intracellular
956 cAMP (open bar; data from Fig. 6B) and compared to the predictions from the
957 corresponding models (magenta). Furthermore, the resting membrane potential of
958 two models is shown that simulate only the membrane depolarization (V_m-*model*;
959 light brown) or only the decreased membrane resistance (R_m-*model*; blue) caused by
960 open HCN channels.

(D) Same comparison between measured values and predictions from the models for the apparent input resistance of cMFBs.

(E) Measured changes of conduction velocity in mossy fibers compared to the predictions by the different models (as in C and D). *Inset top:* Illustration of the model of a mossy fiber with the stimulation positions and the action potentials at two different positions with (magenta line) and without (dashed magenta line) the HH model of HCN channels.

(F) The calculated metabolic costs for maintaining the resting membrane potential are shown for each model as the number of required ATP molecules per mm of mossy fiber axon and per s. The metabolic cost for the firing of a single action potential (AP) is indicated by the dashed line as the number of required ATP molecules per mm of mossy fiber axon (this number was very similar for all models).

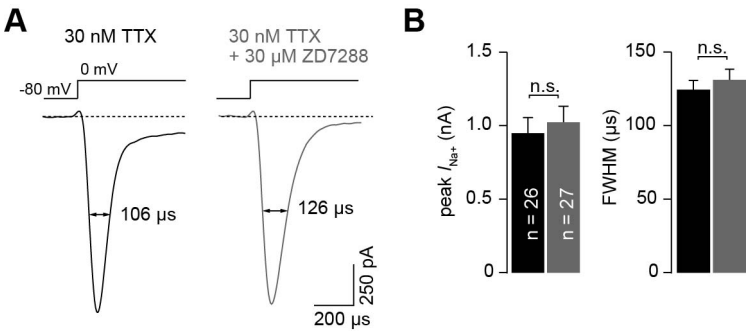

Supplemental Figure S1. ZD7288 does not alter Na^+ currents in cMFBs

(A) Example whole-cell Na^+ currents measured under control conditions (30 nM TTX) and in the presence of additional 30 µM ZD7288 elicited by voltage steps from –80 mV to 0 mV.

(B) With 30 nM TTX present in the extracellular solution (see methods), the average Na^+ current amplitude was 947.9 ± 107.5 pA (n = 26). In the presence of 30 nM TTX and 30 µM ZD7288, the amplitude was not different compared with the currents recorded in 30 nM TTX only (1022.5 ± 109.0 pA; n = 27; $P_{T\text{-}Test} = 0.63$). The average half-duration was 124.3 ± 6.2 µs and 131.5 ± 7.2 µs ($P_{T\text{-}Test} = 0.45$) for control recordings and those performed in the presence of 30 µM ZD7288, respectively.

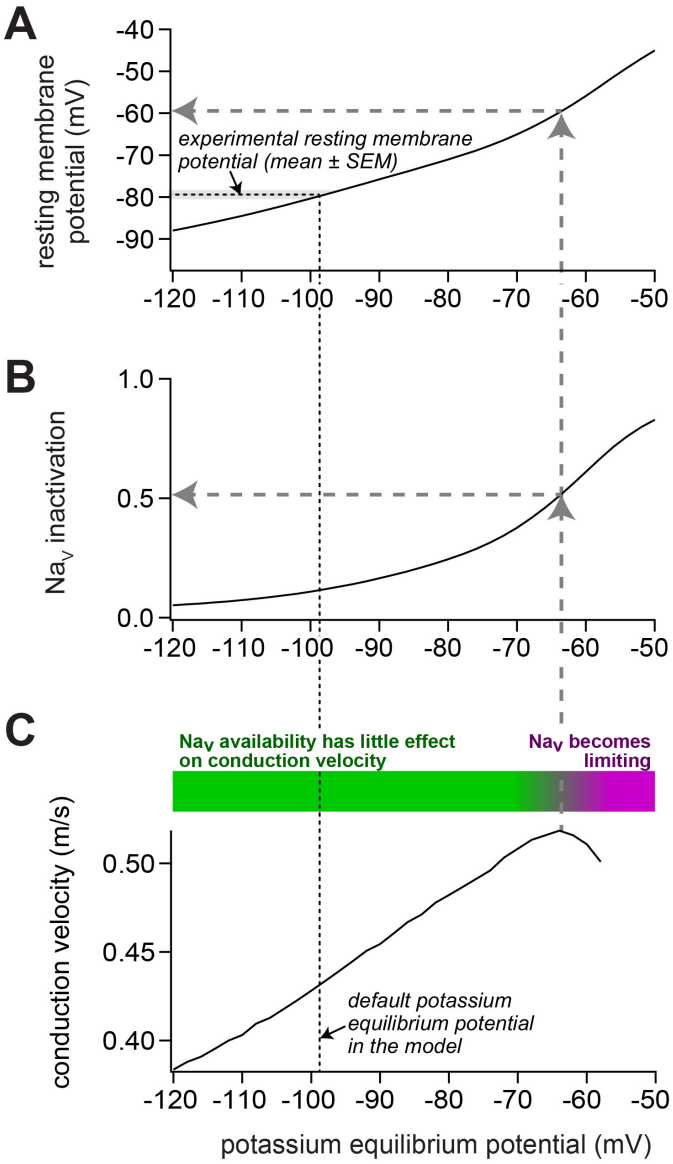

Supplemental Figure S2. Impact of depolarization on Na_V availability and on conduction velocity in our model of a mossy fiber axon

(A) To change the resting membrane potential, the potassium equilibrium potential was varied between –120 and –50 mV. In the default model, the experimentally observed resting membrane potential (indicated by horizontal black dashed line and grey bar; mean ± SEM) was obtained with a potassium equilibrium potential of –98 mV (vertical black dashed line).

(B) Upon depolarization, the inactivation of voltage-dependent sodium (Na_V) channels increased. For the control model, the Na_V inactivation was 12%. For the model reproducing the experiments with ZD7288 and 1 mM intracellular cAMP, the Na_V inactivation was 6 and 17%, respectively. Because the steady-state Na_V availability

depends mostly on the resting membrane potential, the relation between resting membrane potential and Na_V availability was identical for all three models (data not shown).

(C) Upon depolarization, the conduction velocity increased up to a potassium equilibrium potential of about –65 mV (vertical grey dashed arrow), corresponding to an Na_V availability of about 50% (horizontal grey dashed arrow in panel B) and a resting membrane potential of about –60 mV (horizontal grey dashed arrow in panel A). Thus, despite increasing Na_V inactivation, the conduction velocity increased in this range (illustrated by green bar). With stronger depolarization, the conduction velocity declined, indicating that the Na_V availability becomes limiting for conduction velocity (magenta bar).

Supplemental video 1 (video1.mp4). Reconstructed cMFB with labelled synapses and HCN2 channels

3D rendering of a part of a reconstructed cMFB (red) with identified synapses (blue) and HCN2 labeled with gold particles (yellow) based on immune-gold electron microscopic images.

References

Aponte, Y., Lien, C.C., Reisinger, E., and Jonas, P. (2006). Hyperpolarization-activated cation channels in fast-spiking interneurons of rat hippocampus. J Physiol 574, 229-243.

Bacskai, B.J., Hochner, B., Mahaut-Smith, M., Adams, S.R., Kaang, B.K., Kandel, E.R., and Tsien, R.Y. (1993). Spatially resolved dynamics of cAMP and protein kinase A subunits in Aplysia sensory neurons. Science 260, 222-226.

Baginskas, A., Palani, D., Chiu, K., and Raastad, M. (2009). The H-current secures action potential transmission at high frequencies in rat cerebellar parallel fibers. Eur J Neurosci 29, 87-96.

Baker, M., Bostock, H., Grafe, P., and Martius, P. (1987). Function and distribution of three types of rectifying channel in rat spinal root myelinated axons. J Physiol 383.

Baker, M.R., and Edgley, S.A. (2006). Non-uniform olivocerebellar conduction time in the vermis of the rat cerebellum. J Physiol 570, 501-506.

Ballo, A.W., Keene, J.C., Troy, P.J., Goeritz, M.L., Nadim, F., and Bucher, D. (2010). Dopamine modulates Ih in a motor axon. J Neurosci 30, 8425-8434.

Ballo, A.W., Nadim, F., and Bucher, D. (2012). Dopamine modulation of Ih improves temporal fidelity of spike propagation in an unmyelinated axon. J Neurosci 32, 5106-5119.

Basheer, R., Strecker, R.E., Thakkar, M.M., and McCarley, R.W. (2004). Adenosine and sleep-wake regulation. Prog Neurobiol 73, 379-396.

Battefeld, A., Tran, B.T., Gavrilis, J., Cooper, E.C., and Kole, M.H. (2014). Heteromeric $K_v7.2/7.3$ channels differentially regulate action potential initiation and conduction in neocortical myelinated axons. J Neurosci 34, 3719-3732.

Beaumont, V., and Zucker, R.S. (2000). Enhancement of synaptic transmission by cyclic AMP modulation of presynaptic Ih channels. Nat Neurosci 3, 133-141.

Bender, K.J., Ford, C.P., and Trussell, L.O. (2010). Dopaminergic modulation of axon initial segment calcium channels regulates action potential initiation. Neuron 68, 500-511.

Biel, M., Wahl-Schott, C., Michalakis, S., and Zong, X. (2009). Hyperpolarization-activated cation channels: from genes to function. Physiol Rev 89, 847-885.

Birch, B.D., Kocsis, J.D., Di Gregorio, F., Bhisitkul, R.B., and Waxman, S.G. (1991). A voltage- and time-dependent rectification in rat dorsal spinal root axons. J Neurophysiol 66, 719-728.

Börner, S., Schwede, F., Schlipp, A., Berisha, F., Calebiro, D., Lohse, M.J., and Nikolaev, V.O. (2011). FRET measurements of intracellular cAMP concentrations and cAMP analog permeability in intact cells. Nature protocols 6, 427-438.

Boyle, P.J., Scott, J.C., Krentz, A.J., Nagy, R.J., Comstock, E., and Hoffman, C. (1994). Diminished brain glucose metabolism is a significant determinant for falling rates of systemic glucose utilization during sleep in normal humans. J Clin Invest 93, 529-535.

Braitenberg, V., Heck, D., and Sultan, F. (1997). The detection and generation of sequences as a key to cerebellar function: Experiments and theory. Behav Brain Sci 20, 229-&.

Bruce, J.I.E., Straub, S.V., and Yule, D.I. (2003). Crosstalk between cAMP and Ca^{2+} signaling in non-excitable cells. Cell Calcium 34, 431-444.

1064 Burke, K.J., Jr., Keeshen, C.M., and Bender, K.J. (2018). Two forms of synaptic
1065 depression produced by differential neuromodulation of presynaptic calcium
1066 channels. Neuron 99, 969-984.
1067 Buzsáki, G., Logothetis, N., and Singer, W. (2013). Scaling brain size, keeping timing:
1068 evolutionary preservation of brain rhythms. Neuron 80, 751-764.
1069 Canto, C.B., Onuki, Y., Bruinsma, B., van der Werf, Y.D., and De Zeeuw, C.I. (2017).
1070 The Sleeping Cerebellum. Trends Neurosci 40, 309-323.
1071 Caporale, N., and Dan, Y. (2008). Spike timing-dependent plasticity: a Hebbian
1072 learning rule. Annu Rev Neurosci 31, 25-46.
1073 Cardona, A., Saalfeld, S., Schindelin, J., Arganda-Carreras, I., Preibisch, S., Longair,
1074 M., Tomancak, P., Hartenstein, V., and Douglas, R.J. (2012). TrakEM2 software for
1075 neural circuit reconstruction. PLoS One 7, e38011.
1076 Carp, J.S., Tennissen, A.M., and Wolpaw, J.R. (2003). Conduction velocity is inversely
1077 related to action potential threshold in rat motoneuron axons. Exp Brain Res 150,
1078 497-505.
1079 Chadderton, P., Margrie, T.W., and Häusser, M. (2004). Integration of quanta in
1080 cerebellar granule cells during sensory processing. Nature 428, 856-860.
1081 Chaplan, S.R., Guo, H.-Q., Lee, D.H., Luo, L., Liu, C., Kuei, C., Velumian, A.A.,
1082 Butler, M.P., Brown, S.M., and Dubin, A.E. (2003). Neuronal hyperpolarization-
1083 activated pacemaker channels drive neuropathic pain. J Neurosci 23, 1169-1178.
1084 Chéreau, R., Saraceno, G.E., Angibaud, J., Cattaert, D., and Nägerl, U.V. (2017).
1085 Superresolution imaging reveals activity-dependent plasticity of axon morphology
1086 linked to changes in action potential conduction velocity. Proc Natl Acad Sci USA
1087 114, 1401-1406.
1088 Cheung, U., Atwood, H.L., and Zucker, R.S. (2006). Presynaptic effectors contributing
1089 to cAMP-induced synaptic potentiation in Drosophila. J Neurobiol 66, 273-280.
1090 Chevaleyre, V., and Castillo, P.E. (2002). Assessing the role of Ih channels in synaptic
1091 transmission and mossy fiber LTP. Proc Natl Acad Sci U S A 99, 9538-9543.
1092 Cuttle, M.F., Rusznák, Z., Wong, A.Y.C., Owens, S., and Forsythe, I.D. (2001).
1093 Modulation of a presynaptic hyperpolarization-activated cationic current (I_h) at an
1094 excitatory synaptic terminal in the rat auditory brainstem. The Journal of Physiology
1095 534, 733-744.
1096 Debanne, D., Campanac, E., Bialowas, A., Carlier, E., and Alcaraz, G. (2011). Axon
1097 physiology. Physiol Rev 91, 555-602.
1098 Delvendahl, I., and Hallermann, S. (2016). The cerebellar mossy fiber synapse as a
1099 model for high-frequency transmission in the mammalian CNS. Trends Neurosci 39,
1100 722-737.
1101 Delvendahl, I., Jablonski, L., Baade, C., Matveev, V., Neher, E., and Hallermann, S.
1102 (2015). Reduced endogenous Ca^{2+} buffering speeds active zone Ca^{2+} signaling. Proc
1103 Natl Acad Sci USA 112, E3075-3084.
1104 DiFrancesco, D. (2006). Funny channels in the control of cardiac rhythm and mode of
1105 action of selective blockers. Pharmacol Res 53, 399-406.
1106 Elgueta, C., Köhler, J., and Bartos, M. (2015). Persistent discharges in dentate gyrus
1107 perisoma-inhibiting interneurons require hyperpolarization-activated cyclic
1108 nucleotide-gated channel activation. J Neurosci 35, 4131-4139.
1109 Engel, D., and Jonas, P. (2005). Presynaptic action potential amplification by voltage-
1110 gated Na^+ channels in hippocampal mossy fiber boutons. Neuron 45, 405-417.

1111 Fledrich, R., Stassart, R.M., Klink, A., Rasch, L.M., Prukop, T., Haag, L., Czesnik, D.,
1112 Kungl, T., Abdelaal, T.A., Keric, N., *et al.* (2014). Soluble neuregulin-1 modulates
1113 disease pathogenesis in rodent models of Charcot-Marie-Tooth disease 1A. Nat Med
1114 20, 1055-1061.
1115 Forbes, T.A., and Gallo, V. (2017). All Wrapped Up: Environmental Effects on
1116 Myelination. Trends Neurosci 40, 572-587.
1117 Ford, M.C., Alexandrova, O., Cossell, L., Stange-Marten, A., Sinclair, J., Kopp-
1118 Scheinpflug, C., Pecka, M., Attwell, D., and Grothe, B. (2015). Tuning of Ranvier
1119 node and internode properties in myelinated axons to adjust action potential timing.
1120 Nat Commun 6, 8073.
1121 Gentet, L.J., Stuart, G.J., and Clements, J.D. (2000). Direct measurement of specific
1122 membrane capacitance in neurons. Biophys J 79, 314-320.
1123 George, M.S., Abbott, L.F., and Siegelbaum, S.A. (2009). HCN hyperpolarization-
1124 activated cation channels inhibit EPSPs by interactions with M-type K^+ channels.
1125 Nat Neurosci 12, 577-584.
1126 Geurts, F.J., Schutter, E., and Timmermans, J.-P. (2002). Localization of 5-HT2A, 5-
1127 HT3, 5-HT5A and 5-HT7 receptor-like immunoreactivity in the rat cerebellum. J
1128 Chem Neuroanat 24, 65-74.
1129 Golding, N.L., and Oertel, D. (2012). Synaptic integration in dendrites: exceptional
1130 need for speed. The Journal of Physiology 590, 5563-5569.
1131 Grafe, P., Quasthoff, S., Grosskreutz, J., and Alzheimer, C. (1997). Function of the
1132 hyperpolarization-activated inward rectification in nonmyelinated peripheral rat and
1133 human axons. J Neurophysiol 77, 421-426.
1134 Greenberg, S.M., Bernier, L., and Schwartz, J.H. (1987). Distribution of cAMP and
1135 cAMP-dependent protein kinases in Aplysia sensory neurons. J Neurosci 7, 291-301.
1136 Hallermann, S., de Kock, C.P., Stuart, G.J., and Kole, M.H. (2012). State and location
1137 dependence of action potential metabolic cost in cortical pyramidal neurons. Nat
1138 Neurosci 15, 1007-1014.
1139 Hallermann, S., Pawlu, C., Jonas, P., and Heckmann, M. (2003). A large pool of
1140 releasable vesicles in a cortical glutamatergic synapse. Proc Natl Acad Sci U S A
1141 100, 8975-8980.
1142 Harnett, M.T., Magee, J.C., and Williams, S.R. (2015). Distribution and function of
1143 HCN channels in the apical dendritic tuft of neocortical pyramidal neurons. J
1144 Neurosci 35, 1024-1037.
1145 Heck, D., Sultan, F., and Braitenberg, V. (2001). Sequential stimulation of rat cerebellar
1146 granular layer in vivo: Further evidence of a 'tidal-wave' timing mechanism in the
1147 cerebellum. Neurocomputing 38, 641-646.
1148 Hodgkin, A.L., and Huxley, A.F. (1952). A quantitative description of membrane
1149 current and its application to conduction and excitation in nerve. J Physiol 117, 500-
1150 544.
1151 Hore, J., Wild, B., and Diener, H.C. (1991). Cerebellar dysmetria at the elbow, wrist,
1152 and fingers. J Neurophysiol 65, 563-571.
1153 Horn, S., Quasthoff, S., Grafe, P., Bostock, H., Renner, R., and Schrank, B. (1996).
1154 Abnormal axonal inward rectification in diabetic neuropathy. Muscle Nerve 19,
1155 1268-1275.
1156 Howells, J., Bostock, H., and Burke, D. (2016). Accommodation to hyperpolarization of
1157 human axons assessed in the frequency domain. J Neurophysiol 116, 322-335.

Howells, J., Trevillion, L., Bostock, H., and Burke, D. (2012). The voltage dependence of I_h in human myelinated axons. J Physiol 590, 1625-1640.

Huang, H., and Trussell, L.O. (2014). Presynaptic HCN channels regulate vesicular glutamate transport. Neuron 84, 340-346.

Huang, Z., Lujan, R., Kadurin, I., Uebele, V.N., Renger, J.J., Dolphin, A.C., and Shah, M.M. (2011). Presynaptic HCN1 channels regulate $Ca_v3.2$ activity and neurotransmission at select cortical synapses. Nat Neurosci 14, 478-486.

Hummert, S., Thon, S., Eick, T., Schmauder, R., Schulz, E., and Benndorf, K. (2018). Activation gating in HCN2 channels. PLoS Comput Biol 14, e1006045.

Isope, P., Dieudonne, S., and Barbour, B. (2002). Temporal organization of activity in the cerebellar cortex: a manifesto for synchrony. Ann N Y Acad Sci 978, 164-174.

Jack, J.J.B., Noble, D., and Tsien, R.W. (1983). Electric current flow in excitable cells. (Oxford: Clarendon Press).

Jankelowitz, S.K., Howells, J., and Burke, D. (2007). Plasticity of inwardly rectifying conductances following a corticospinal lesion in human subjects. J Physiol 581, 927-940.

Kim, J.H., and von Gersdorff, H. (2012). Suppression of spikes during posttetanic hyperpolarization in auditory neurons: the role of temperature, I_h currents, and the Na^+-K^+-ATPase pump. J Neurophysiol 108, 1924-1932.

Ko, K.W., Rasband, M.N., Meseguer, V., Kramer, R.H., and Golding, N.L. (2016). Serotonin modulates spike probability in the axon initial segment through HCN channels. Nat Neurosci 19, 826-834.

Kole, M.H., Hallermann, S., and Stuart, G.J. (2006). Single Ih channels in pyramidal neuron dendrites: properties, distribution, and impact on action potential output. J Neurosci 26, 1677-1687.

Koschinski, A., and Zaccolo, M. (2017). Activation of PKA in cell requires higher concentration of cAMP than in vitro: implications for compartmentalization of cAMP signalling. Scientific reports 7, 14090.

Lang, E.J., and Rosenbluth, J. (2003). Role of myelination in the development of a uniform olivocerebellar conduction time. J Neurophysiol 89, 2259-2270.

Lin, C.S., Krishnan, A.V., Lee, M.J., Zagami, A.S., You, H.L., Yang, C.C., Bostock, H., and Kiernan, M.C. (2008). Nerve function and dysfunction in acute intermittent porphyria. Brain 131, 2510-2519.

Lorenz, C., and Jones, K.E. (2014). I_H activity is increased in populations of slow versus fast motor axons of the rat. Front Hum Neurosci 8, 766.

Magee, J.C. (1999). Dendritic I_h normalizes temporal summation in hippocampal CA1 neurons. Nat Neurosci 2, 508–514.

Maiellaro, I., Lohse, M.J., Kittel, R.J., and Calebiro, D. (2016). cAMP signals in Drosophila motor neurons are confined to single synaptic boutons. Cell Reports 17, 1238-1246.

Marder, E., and Bucher, D. (2001). Central pattern generators and the control of rhythmic movements. Curr Biol 11, R986-996.

Mathews, P.J., Jercog, P.E., Rinzel, J., Scott, L.L., and Golding, N.L. (2010). Control of submillisecond synaptic timing in binaural coincidence detectors by K_v1 channels. Nat Neurosci 13, 601-609.

Matsubara, A., Laake, J.H., Davanger, S., Usami, S.-i., and Ottersen, O.P. (1996). Organization of AMPA receptor subunits at a glutamate synapse: a quantitative

immunogold analysis of hair cell synapses in the rat organ of Corti. J Neurosci 16, 4457-4467.

McKenzie, I.A., Ohayon, D., Li, H.L., de Faria, J.P., Emery, B., Tohyama, K., and Richardson, W.D. (2014). Motor skill learning requires active central myelination. Science 346, 318-322.

Momin, A., and McNaughton, P.A. (2009). Regulation of firing frequency in nociceptive neurons by pro-inflammatory mediators. Exp Brain Res 196, 45-52.

Nicholas, A.P., Pieribone, V.A., and Hökfelt, T. (1993). Cellular localization of messenger RNA for beta-1 and beta-2 adrenergic receptors in rat brain: an in situ hybridization study. Neuroscience 56, 1023-1039.

Notomi, T., and Shigemoto, R. (2004). Immunohistochemical localization of I_h channel subunits, HCN1-4, in the rat brain. J Comp Neurol 471, 241-276.

Nusser, Z. (2012). Differential subcellular distribution of ion channels and the diversity of neuronal function. Curr Opin Neurobiol 22, 366-371.

Palay, S.M., and Chan-Palay, V. (1974). Cerebellar cortex: cytology and organization (Springer, Berlin).

Pape, H.C., and McCormick, D.A. (1989). Noradrenaline and serotonin selectively modulate thalamic burst firing by enhancing a hyperpolarization-activated cation current. Nature 340, 715-718.

Person, A.L., and Raman, I.M. (2012). Synchrony and neural coding in cerebellar circuits. Front Neural Circuits 6, 97.

Porkka-Heiskanen, T., Strecker, R.E., Thakkar, M., Bjorkum, A.A., Greene, R.W., and McCarley, R.W. (1997). Adenosine: a mediator of the sleep-inducing effects of prolonged wakefulness. Science 276, 1265-1268.

Press, W.H., Teukolsky, S.A., Vetterling, W.T., and Flannery, B.P. (2002). Numerical recipes in C++: the art of scientific computing, 2nd edn (Cambridge, UK: Cambridge UP).

Rama, S., Zbili, M., Bialowas, A., Fronzaroli-Molinieres, L., Ankri, N., Carlier, E., Marra, V., and Debanne, D. (2015). Presynaptic hyperpolarization induces a fast analogue modulation of spike-evoked transmission mediated by axonal sodium channels. Nat Commun 6, 10163.

Rancz, E.A., Ishikawa, T., Duguid, I., Chadderton, P., Mahon, S., and Häusser, M. (2007). High-fidelity transmission of sensory information by single cerebellar mossy fibre boutons. Nature 450, 1245-1248.

Ritzau-Jost, A., Delvendahl, I., Rings, A., Byczkowicz, N., Harada, H., Shigemoto, R., Hirrlinger, J., Eilers, J., and Hallermann, S. (2014). Ultrafast action potentials mediate kilohertz signaling at a central synapse. Neuron 84, 152-163.

Robinson, R.B., and Siegelbaum, S.A. (2003). Hyperpolarization-activated cation currents: from molecules to physiological function. Annu Rev Physiol 65, 453-480.

Salami, M., Itami, C., Tsumoto, T., and Kimura, F. (2003). Change of conduction velocity by regional myelination yields constant latency irrespective of distance between thalamus and cortex. Proc Natl Acad Sci U S A 100, 6174-6179.

Sánchez-Soto, M., Bonifazi, A., Cai, N.S., Ellenberger, M.P., Newman, A.H., Ferré, S., and Yano, H. (2016). Evidence for noncanonical neurotransmitter activation: norepinephrine as a dopamine D2-Like receptor agonist. Mol Pharmacol 89, 457-466.

Santoro, B., Chen, S., Luthi, A., Pavlidis, P., Shumyatsky, G.P., Tibbs, G.R., and Siegelbaum, S.A. (2000). Molecular and functional heterogeneity of

hyperpolarization-activated pacemaker channels in the mouse CNS. J Neurosci 20, 5264-5275.

Schmidt-Hieber, C., and Bischofberger, J. (2010). Fast Sodium Channel Gating Supports Localized and Efficient Axonal Action Potential Initiation. J Neurosci 30, 10233-10242.

Schweighofer, N., Doya, K., and Kuroda, S. (2004). Cerebellar aminergic neuromodulation: towards a functional understanding. Brain Res Brain Res Rev 44, 103-116.

Softky, W. (1994). Sub-millisecond coincidence detection in active dendritic trees. Neuroscience 58, 13-41.

Soleng, A.F., Chiu, K., and Raastad, M. (2003). Unmyelinated axons in the rat hippocampus hyperpolarize and activate an H current when spike frequency exceeds 1 Hz. J Physiol 552, 459-470.

Sugihara, I., Lang, E.J., and Llinás, R. (1993). Uniform olivocerebellar conduction time underlies Purkinje cell complex spike synchronicity in the rat cerebellum. The Journal of Physiology 470, 243-271.

Swadlow, H.A., and Waxman, S.G. (2012). Axonal conduction delays. Scholarpedia 7, 1451 doi:1410.4249/scholarpedia.1451.

Tang, Z.Q., and Trussell, L.O. (2015). Serotonergic regulation of excitability of principal cells of the dorsal cochlear nucleus. J Neurosci 35, 4540-4551.

Thon, S., Schmauder, R., and Benndorf, K. (2013). Elementary functional properties of single HCN2 channels. Biophys J 105, 1581-1589.

Townsend, R.E., Prinz, P.N., and Obrist, W.D. (1973). Human cerebral blood flow during sleep and waking. J Appl Physiol 35, 620-625.

Trevisiol, A., Saab, A.S., Winkler, U., Marx, G., Imamura, H., Mobius, W., Kusch, K., Nave, K.A., and Hirrlinger, J. (2017). Monitoring ATP dynamics in electrically active white matter tracts. eLife 6.

Wang, J., Chen, S., and Siegelbaum, S.A. (2001). Regulation of hyperpolarization-activated HCN channel gating and cAMP modulation due to interactions of COOH terminus and core transmembrane regions. The Journal of General Physiology 118, 237-250.

Waxman, S.G., Kocsis, J.D., and Stys, P.K. (1995). The Axon: Structure, Function, and Pathophysiology (Oxford University Press).

Waxman, S.G., and Ritchie, J.M. (1993). Molecular dissection of the myelinated axon. Ann Neurol 33, 121-136.

Wickenden, A.D., Maher, M.P., and Chaplan, S.R. (2009). HCN pacemaker channels and pain: a drug discovery perspective. Curr Pharm Des 15, 2149-2168.

Williams, S.R., and Stuart, G.J. (2000). Site independence of EPSP time course is mediated by dendritic I_h in neocortical pyramidal neurons. J Neurophysiol 83, 3177-3182.

Wu, X., Liao, L., Liu, X., Luo, F., Yang, T., and Li, C. (2012). Is ZD7288 a selective blocker of hyperpolarization-activated cyclic nucleotide-gated channel currents? Channels (Austin) 6, 438-442.

Yang, J., Ye, M., Tian, C., Yang, M., Wang, Y., and Shu, Y. (2013). Dopaminergic modulation of axonal potassium channels and action potential waveform in pyramidal neurons of prefrontal cortex. J Physiol 591, 3233-3251.

1299 Yin, L., Rasch, M.J., He, Q., Wu, S., Dou, F., and Shu, Y. (2017). Selective modulation
1300 of axonal sodium channel subtypes by 5-HT1A receptor in cortical pyramidal
1301 neuron. Cereb Cortex 27, 509-521.
1302 Zagotta, W.N., Olivier, N.B., Black, K.D., Young, E.C., Olson, R., and Gouaux, E.
1303 (2003). Structural basis for modulation and agonist specificity of HCN pacemaker
1304 channels. Nature 425, 200-205.
1305